CHAPTER 2

EXPERIMENTAL APPARATUS AND TECHNIQUES

2.1 THE DISCHARGE AND VACUUM SYSTEMS

Pyrex glass discharge chambers have been used for the present study of sparks and d.c. discharges in SF_6 because of their amenability to optical diagnostic techniques. The chambers were designed so that they could be readily dismantled, cleaned and reassembled. This was done because discharges through SF_6 generate the gradual build-up of fluoride compounds on the electrode surfaces and glass walls, making regular cleaning important.

It has been necessary to use two different discharge chambers because of the incompatibility of some of the diagnostic techniques with one particular chamber design.

The first chamber consists of a cylindrical Pyrex tube of length 1.00 metre and inner diameter 2.7 cm with two stainless steel ring electrodes mounted at either end, coaxial with the tube. A short side-arm of internal diameter 1 cm which is terminated with a fused silica window, is connected to the discharge tube midway along its length. The electrodes, supported in metallic mounts, are arranged so that their inner surfaces are flush with the inside wall of the discharge tube. The mounts themselves serve also to securely couple this tube to Pyrex tubing on either end such that the extensions are coaxial with the discharge tube (Fig. 2.1.1). The mechanical connections are made with brass couplings and 'O'-ring (Viton) seals. The short extension tube on one end of the discharge tube is sealed with a planar fused silica window. The window has a transmittance curve that extends down to about 220 nm and allows the cathode to be illuminated with ultraviolet radiation from a commercial mercury-neon (Pen-Ray, Model 11SC-1) lamp. This allows the statistical time lag to breakdown to be eliminated. The extension tube connected to the other end of the discharge tube is 30 cm long, flares out to a diameter of 50 mm and is terminated with a fused silica window similar to that described above. Connected to this extension tube are side arms to the vacuum pumps, pressure gauges and gas-inlet systems. The larger diameter of this tube prevents reflections

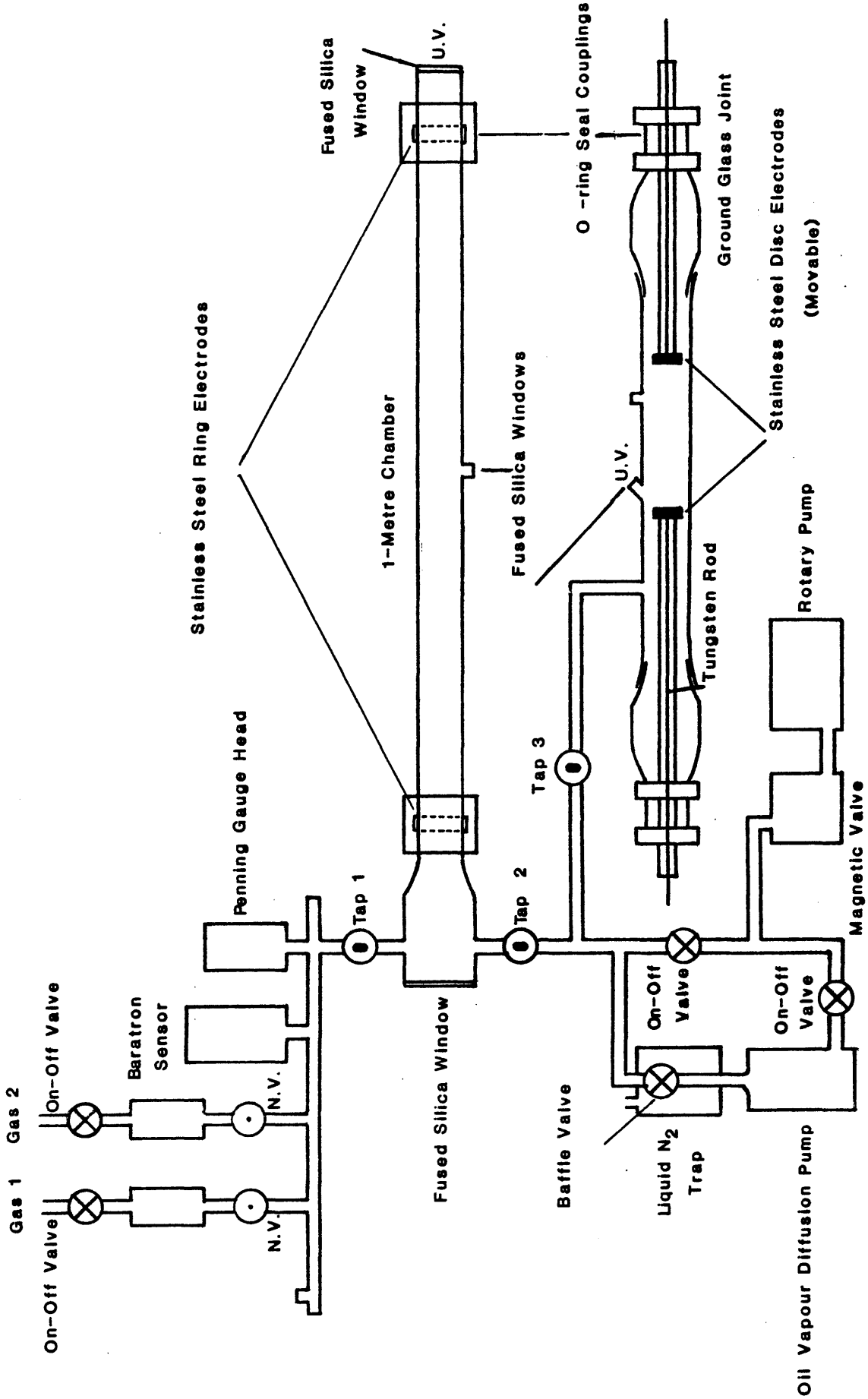

Fig. 2.1.1 Schematic diagram showing the discharge and vacuum systems. Also shown are the gas inlet system and pressure gauges.

from imperfections in the glassware in the vicinity of the side-arm entrances, when a laser beam is passed through the discharge tube along an axial path near the tube wall. This is important in the laser interferometry work to be described later.

The second discharge chamber consists of a cylindrical Pyrex tube of length 58 cm and inner diameter 2.6 cm. The electrode units consist of a couple of 2.45 cm diameter stainless steel disc electrodes screwed onto the ends of two tungsten rods which can be moved axially down the discharge tube. The rods themselves are encased in glass sleeving to prevent discharges 'striking' to them. In connection with a particular experiment in this chamber regarding the glow-arc transition in SF_6, a different cathode configuration is used. This consists of a thin, 1 cm diameter stainless steel disc embedded centrally in the face of a machinable ceramic disc of diameter 2.45 cm such that the steel disc face is coplanar with that of the ceramic to within 10 μm (as evidenced from electron microscope photographs). The pair of tungsten rods holding anode and cathode, are attached to the discharge tube, each by means of a ground-glass joint and a double 'O'-ring coupling device (Fig. 2.1.1), both of which have been designed to provide good vacuum sealing and to allow smooth axial movement of the anode and cathode. The ground glass joints together with all 'O'-ring couplings are made vacuum tight by using a low vapour pressure grease (Apiezon, type N). The electrode separation in this discharge chamber could be made as large as 40 cm, but for most experiments a gap length of less than or equal to 20 cm was selected. Gap lengths were measured to the nearest millimetre, using a scale taped to the Pyrex tube. Parallax errors in these measurements were minimal because of the comparatively large electrodes used. Connected to the discharge tube are two short side arms of internal diameter, 1 cm. One of these is inclined at an angle of about 50^0 to the tube axis and is sealed with a fused silica window which allows the cathode to be irradiated using an externally located ultraviolet (Pen-Ray) lamp.

The other side arm positioned some 8 cm from the first is at right angles to the tube axis. It incorporates a ground glass joint at its open end, which allows a thermocouple or Langmuir probe to be inserted into the discharge gap. Alternatively, a fused silica window can be located at this side arm for spectroscopic analysis.

As shown in Fig. 2.1.1, the two discharge chambers are connected in parallel to a gas inlet system, pressure gauges and a pumping unit.

Two gas-inlet lines are used to allow both the study of SF_6 and SF_6/Ar mixtures. C.P. grade SF_6 (Matheson) of 99.8% purity and Argon (C.I.G.) of 99.99% purity are used. Clean, outgassed copper piping of 3 mm inner diameter is used to connect the gas cylinders via their pressure regulators to the discharge chambers. High vacuum "on-off" valves and needle valves (Edwards) are used in the gas lines to control filling pressures. This control was improved by reducing the pressure differential across the needle valves by using 50 ml brass cylinders on the high pressure side of the needle valves. All valve-piping connections in the two gas lines employ 'O'-ring (Viton) seals.

The filling pressures used in the discharge tubes are measured with a capacitance manometer (MKS Baratron, type 222). This type of pressure gauge has the advantage over other conventional vacuum gauges, in being able to measure absolute pressures directly, independent of gas or vapour composition. This makes it ideal for use with gas mixtures. A pressure transducer unit built in with the variable capacitance sensor head is activated by a power supply and produces a d.c. voltage signal numerically equal to the system pressure in Torr. This signal is displayed on an accurately zeroed digital voltmeter (Fluke, type 8000 A). The manometer is capable of measuring to within 2%, all pressures from 1×10^{-3} Torr to 10 Torr. A Penning gauge head (Edwards, Model 5MF) previously calibrated for air against a McLeod gauge, is incorporated into the system to measure the background pressure when the discharge chambers are being evacuated. This gauge is capable of reading pressures down to 1×10^{-6} Torr.

The pumping unit (Fig. 2.1.1) comprises a rotary pump (Dynavac, Model 2) capable of evacuating from atmospheric pressure down to less than one micron (1×10^{-3} Torr), and an oil vapour diffusion pump (Dynavac, Model OD-150) capable of further evacuating the system from about 1×10^{-2} Torr down to less than 1×10^{-6} Torr. A liquid N_2 trap is placed between the diffusion pump and the remainder of the vacuum system. A magnetic valve arrangement (Edwards, Model SVAR8-4) is used with the rotary pump to provide automatic isolation of the pump from the vacuum system and diffusion pump, in the event of power failure. Air admittance to the rotary pump occurs simultaneously with isolation.

Before an experimental run, the discharge chamber to be used is dismantled and the tube, electrodes and 'O'-rings are thoroughly washed out with petroleum ether and distilled ethanol. The 'O'-rings are then coated with Apiezon type N grease, while the glassware and electrodes are dried with hot air. The system is then assembled and evacuated continuously until a pressure of 1×10^{-6} Torr is attained. An apparent leak rate of approximately 5 microns per hour is then obtained upon isolation of the vacuum system from the pumping unit. The chamber to be used is filled to the desired pressure and isolated from the rest of the vacuum system by means of glass taps.

2.2 THE ELECTRICAL CIRCUITS

2.2.1 The Spark Circuitry

There are two commonly used methods for the production of spark discharges in the laboratory. One of these is the "coaxial-cable discharge" method, which involves charging up a coaxial line to an appropriate voltage and then discharging it through a specially designed spark chamber into a terminated cable of the same impedance. An advantage of a system based on this technique is that a single oscillographic recording is sufficient to allow an accurate determination of all the electrical parameters appropriate to the spark, as demonstrated by Doran and Meyer (1967). One disadvantage however, is that the coaxial spark chamber has to be metallic and is therefore not suitable for use in the present experiment, for the reasons mentioned in the previous section. An alternative method which has been adopted for the present studies of spark growth in SF_6 and Argon/SF_6 mixtures, employs a charged capacitor to feed sufficient energy into a gap to initiate breakdown. The circuitry used is basically of the same form as others given in the literature (see for example, Tholl, 1967; Lewis and Woolsey, 1981).

Separate circuits of similar form have been used to pulse the two discharge systems. Fig. 2.2.1 illustrates the circuit used to discharge the ring electrode system, with the square-bracketed values representing the components used in the pulsing of the smaller movable electrode system. For ease of discussion, the corresponding components A and B used in the ring-electrode and moveable-electrode systems respectively, will be designated as A/B in the text below. The basic circuit operation is as follows. A stabilized power supply (Brandenburg, Model 800/Hipotronix, Model 810-100) is used to charge a storage capacitor C (2 μF, C.S.I., rated at 15 kV d.c. and < 50 nH) to a desired positive potential $+V_0$ (12 kV/3 kV) through resistors R_1 and R_2. When the hydrogen thyratron (English Electric Valve, Model CX1140/3C45) is made conducting by the application of appropriate grid pulses (discussed below), its anode potential rapidly falls within a few nanoseconds

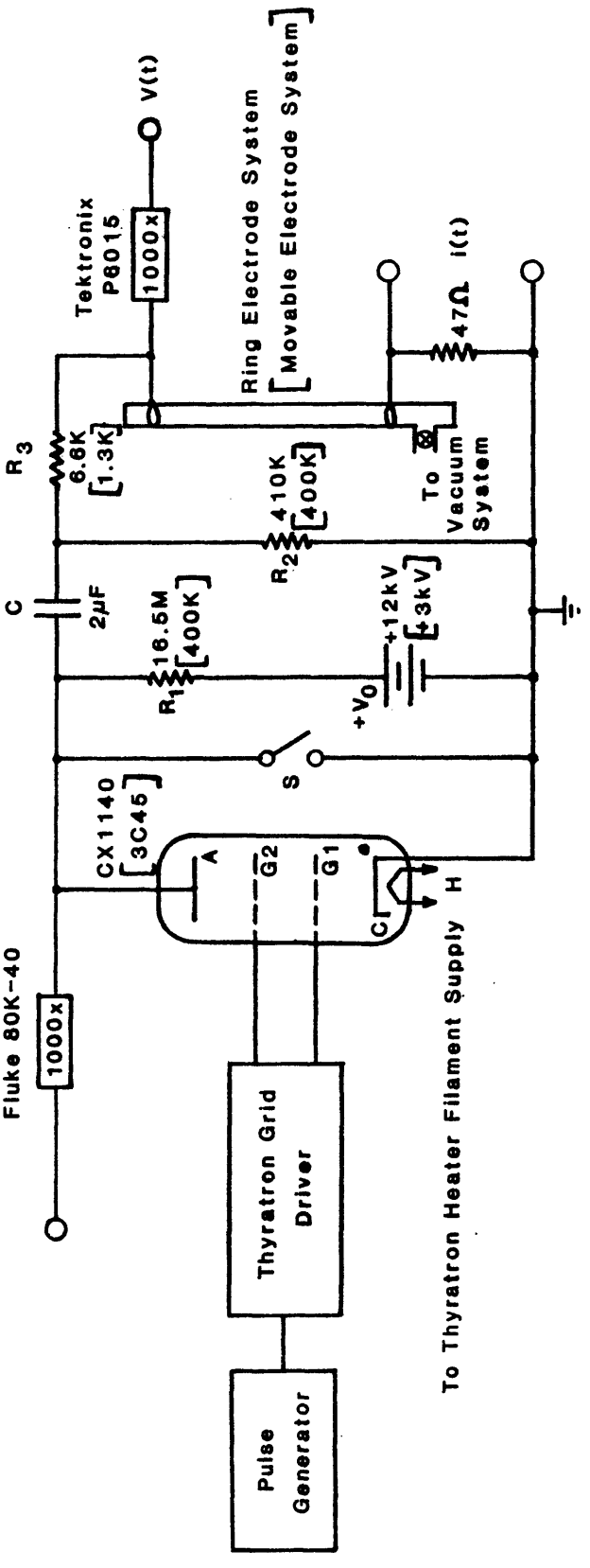

Fig. 2.2.1 The spark circuitry for the metre-chamber and the movable-electrode chamber. The square bracketed circuit components represent those used with the latter chamber.

from $+V_0$ to a value less than +10 volts (i.e. to the thyratron's conduction-maintenance voltage). Since, in this very short time, capacitor C would have discharged to a negligible extent, its negative plate simultaneously falls from ground potential to a value very close to $-V_0$. In this manner the circuit generates a negative voltage step which is directly applied across the discharge gap. If V_0 is sufficiently large (as are the values quoted above), breakdown occurs and the capacitor discharges through the thyratron and the gap. Resistor R_3 (6.6 kΩ/1.3 kΩ) is chosen to limit the current through the gap and to provide a sufficiently large time-constant to allow the various discharge phases following breakdown to be readily observed and studied. Following decay of the spark, the storage capacitor recharges and the circuit is ready to trigger again. The time-constant of the charging circuit is quite long (34 sec/1.6 sec) and so the spark circuit is intended only for "single-shot" operation. A specially designed mechanical safety switch S, with brass electrodes is incorporated in the circuit for discharging residual charge on the capacitor. This switch can also be used as a crude pulsing unit in place of the thyratron as discussed in the next chapter.

The CX1140 hydrogen thyratron, which was originally used in this laboratory for switching kiloampere Z-pinch discharges, is used in the present low current experiments on account of its efficiency and reliability in rapidly switching high voltages. A tetrode thyratron, the CX1140 possesses two grids between anode and cathode. Grid 2, which is nearer the anode, is given a negative bias with respect to grid 1 so that during the interpulse or quiescent phase, efficient anode "hold-off" is achieved. When it is necessary to produce pulses of high repetition rate with minimum jitter, the two grids are conventionally pulsed from separate sources, with a delay of about 1 μs between them. Grid 1 is pulsed first providing conduction between it and the cathode, and when grid 2 is then pulsed, a very rapid and precise take-over of conduction by the anode occurs.

In the grid-drive circuit presently used (Fig. 2.2.2), both grid pulses originate from a common source and are applied simultaneously to the grids. This design may give rise to an increased shot-to-shot variation of 5 ns, in the anode delay time (i.e. in the time for anode conduction after grid 2 has been pulsed), with an increase under specified conditions, of the anode delay time drift from 20 ns to 100 ns. This loss of precision in the timing of anode conduction is likely, however, to only be serious when pulsing at a high repetition rate, or when studying the formative times to breakdown of spark discharges. Since only single-shot operation is employed and since mainly post-breakdown phenomena in SF_6 sparks are investigated (see next chapter), no disadvantages in the use of the grid circuitry of Fig. 2.2.2 arise. Referring to this circuit, the voltage across the secondary transformer (220 V, r.m.s.) at the input stage is rectified, smoothed and approximately doubled in amplitude by the network comprising diodes D_2 and D_3 and capacitors C_1 and C_2. The resulting d.c. voltage signal charges capacitor C_3 through resistor R_3. When the silicon-controlled rectifier switch SCR, is turned on by applying a small positive voltage trigger pulse to its gate, capacitor C_3 discharges through the primary winding of the ferrite-core pulse transformer, P.T. (turns ratio 1:4.3). An oscillatory current is set up, but only a negative pulse appears across the transformer due to the presence of diode D_4. The transformer serves to invert and amplify this pulse, and gives a 1700 V positive-going pulse of 80 ns rise time and 5 μs duration, at its output. Ringing on this pulse is controlled by resistor R_4. The last stage of the circuit channels the pulse to both grids, but due to the extra load presented, the pulses have an amplitude at the thyratron grid pin connections, of 1500 V (with the thyratron disconnected). They have a rate of rise of 1.5 kV per microsecond and a duration of 5 μs. Included in the grid-drive circuit is a variable negative voltage biasing network, consisting of an emitter-follower which is made up of transistor Q and resistors R_1 and R_2. The variable resistor R_1 is preset to provide a d.c. potential of -120 V on

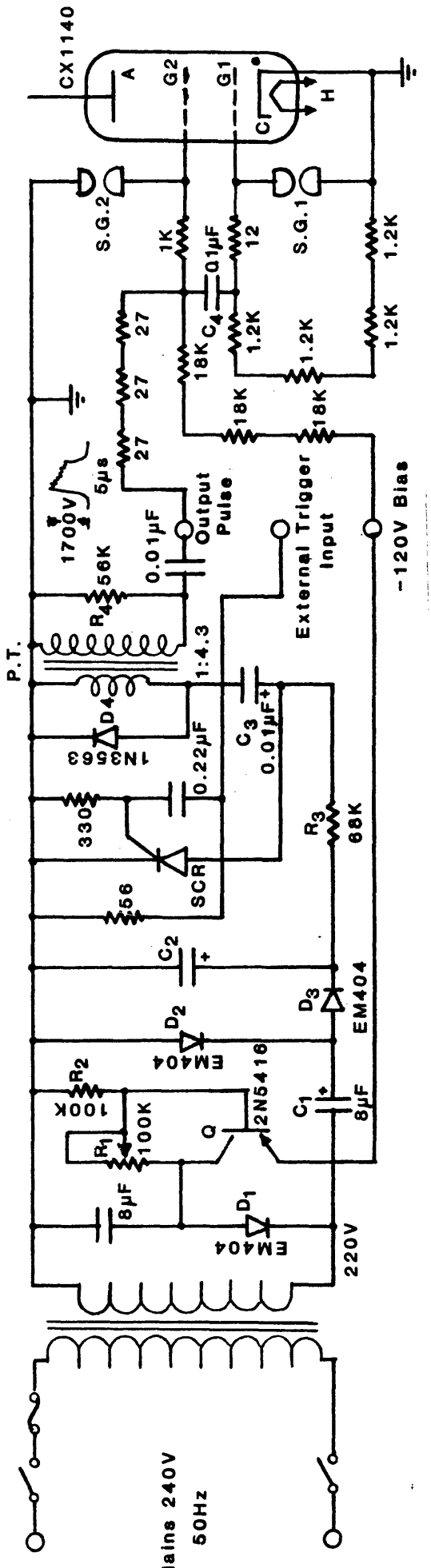

Fig. 2.2.2 The CX1140 thyratron grid-drive circuit.

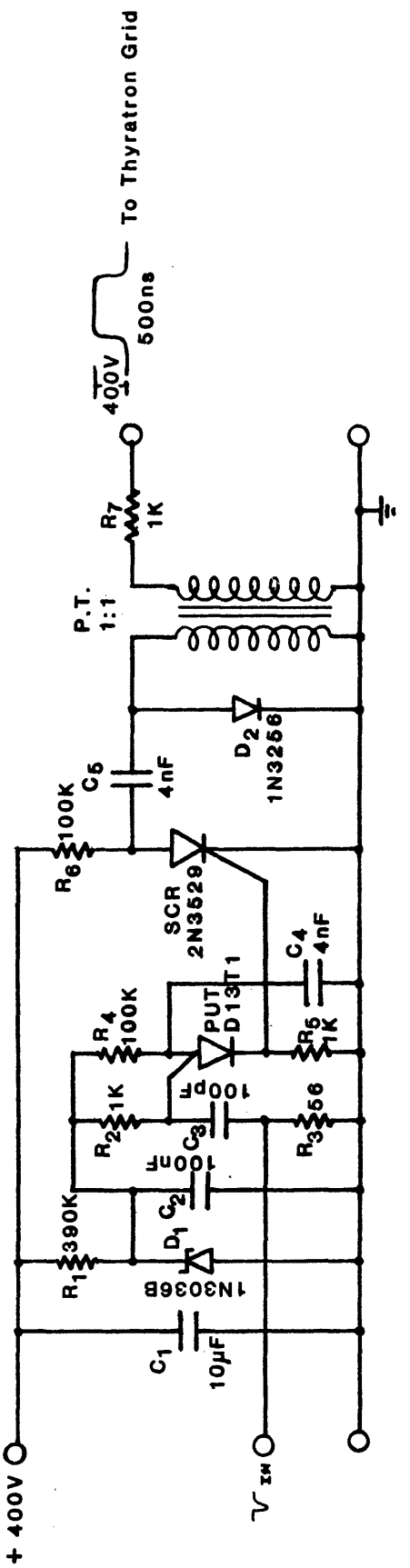

Fig. 2.2.3 The 3C45 thyratron grid-drive circuit.

the emitter lead of the transistor. This negative potential is applied to grid 2 of the thyratron through the resistor chain shown in Fig. 2.2.2, and as already mentioned, provides anode "hold-off" in the quiescent state. Capacitor C_4 serves to externally isolate the grids from one another. At the instant of firing, the grid potentials rise rapidly. Voltage spikes of the order of 20 ns duration, and amplitudes which are an appreciable fraction of the anode voltage (for the present case, this is 12 kV), develop. Because these spikes can sometimes cause breakdown in the grid-drive circuitry, two commercial spark plugs SG1 and SG2 have been connected between the grids and ground. They are accurately set to discharge any spikes larger than 1800 volts in amplitude. The heater filament H, of the thyratron (Fig. 2.2.2) is maintained at a constant voltage (6.3 V, r.m.s.) and current (22 A, r.m.s.) at all times, in order to maintain constant gas pressure and cathode temperature. Throughout the present experiments the grid-drive circuit is activated by triggering it with the output pulse (+5 V, 5 μs duration) of a commercial pulse generator (Cossor, Model 1097).

The hydrogen thyratron used with the small movable-electrode system (EEV, Model 3C45) possesses only one grid and has a maximum peak-forward-voltage rating of +3 kV. A schematic diagram of the circuit used to provide its grid pulse is shown in Fig. 2.2.3. This is somewhat similar to the CX1140 grid-drive circuit, except that there is no biasing network included. In the quiescent state capacitors C_4 and C_5 are charged to 47 V and 400 V respectively. The programmable unijunction transistor PUT switches on when a small negative-going trigger pulse is applied to it. This causes C_4 to discharge through resistor R_5. The voltage step generated across this resistor turns on the silicon-controlled rectifier SCR and allows C_5 to discharge through the primary winding of the pulse transformer P.T. (turns ratio 1:1). A positive-going rectangular-shaped pulse with a 40 ns rise-time, 500 ns duration and peak amplitude of 400 V is thus generated and fed directly to the thyratron grid.

2.2.2 D.C. Discharge Circuitry

Part of the present investigation involves the study of low-current d.c. discharges in SF_6. This study complements the investigations of spark development. Phenomena which are found in particular current regimes of the low pressure SF_6 spark, also exist in d.c. discharges under similar conditions of current and gas pressure. A number of diagnostic techniques have been applied to these d.c. discharges and valuable information,which assists in the interpretation of the behaviour and development of the SF_6 spark, has been obtained. The circuit used to produce a low-current d.c. glow discharge consists of a stabilized power supply connected to the discharge tube via a suitable ballast resistor. Both discharge chambers have been used, with ballast resistors varying in magnitude from 100 kΩ to over 500 kΩ. In most experiments, a Hipotronix,Model 810-100 with reversible polarity and with a rating of 10 kV at 100 mA, is used. However, an A.P.T. Electronic Industries, Model 2140 stabilized power supply with a rating of 2.5 kV at 120 mA and with a floating output is used for Langmuir probe studies as described later.

2.3 THE DIAGNOSTIC TECHNIQUES AND APPARATUS

2.3.1 Measurement of the Electrical Parameters of the SF_6 Spark

The current flowing through the low pressure SF_6 spark has been measured by either recording the voltage pulse developed across a small resistor (47Ω) placed between the discharge-anode and ground, or by means of a commercial current probe (Tektronix, Model P6042) also attached between anode and ground. The results obtained by these two methods are identical, except that current oscillograms obtained using the resistor appear inverted. The current probe is capable of accurately measuring current signals ranging in amplitude from 0.1 mA to 10 A, up to frequencies of 10 MHz.

The total voltage to which the discharge gap is subjected at the instant of thyratron-anode conduction is monitored to an accuracy of ± 10 V on a digital voltmeter (Fluke, Model 8000A) using a calibrated 1000 x attenuator (Fluke, Model 80K-40). This attenuator is specially intended for use with the above voltmeter which has an input impedance of 10 MΩ. The time variation of the gap voltage has been measured using another 1000 X attenuator (Tektronix, Model P6015) connected between cathode and ground (cf. Fig. 2.2.1).

The current and voltage waveforms of a particular spark are displayed simultaneously on a dual-beam oscilloscope (Tektronix, Model 551). Tektronix, type-G plug-in amplifiers are used in conjunction with the oscilloscope. The rise-time of the plug-in amplifier and oscilloscope-mainframe combination is 20 ns while the current and voltage probe-oscilloscope combinations have a rise-time estimated as being no greater than 30 ns. As will be seen later, these risetimes are more than adequate for measurement of the currents and voltages associated with low pressure sparks in SF_6. The oscilloscope is normally triggered externally, using the pulse which activates the thyratron grid-drive circuit (cf. Figures 2.2.2 and 2.2.3), but can also be triggered internally using either the current or voltage waveform. The two type-G plug-in amplifiers are calibrated before use and the high voltage attenuator carefully

compensated with its plug-in unit. The absolute uncertainty in measurements of both current and voltage is estimated as being less than 10%.

For more accurate current and voltage resolution, a Tektronix, type-Z plug-in unit is used. This is a differential voltage comparator, capable of applying a known d.c. voltage to cancel any unwanted component of the applied signal. This allows accurate measurements to be made of relatively small amplitude variations in a large signal. The type-Z unit provides an effective screen height of ± 2000 cm at maximum sensitivity, permitting a maximum resolution of 0.005%.

Oscillograms of current and voltage waveforms are recorded on high speed (3000 ASA) film (Polaroid, type-47) using an oscilloscope camera (Tektronix, Model C-19) fitted with an f/1.9, 75 mm lens.

2.3.2 Laser Interferometric Techniques and Apparatus for Measuring Plasma Refractivity and Radial Refractivity Gradients in SF_6 Sparks

2.3.2.(i) Introduction

Optical interferometry is a well recognised diagnostic tool for the investigation of the properties and behaviour of gas discharges and plasmas. It has the advantage over other techniques such as those using electric probes, magnetic probes and particle beams, in that it does not produce perturbations in the system being investigated.

It has been through the development of the laser, that optical interferometry has achieved great importance as a plasma diagnostic technique. This is because the laser is the only source capable of producing radiation sufficiently intense and monochromatic to compete favourably with the luminosity of a plasma in a narrow spectral band, while simultaneously being an effective collimated source on account of its small beam divergence.

Fundamentally, an optical interferometer is a device used to measure refractive index. It achieves this by comparing the phase of one optical beam with the phase of another which has traversed a different path. This comparison is made by allowing the two beams to interfere and form a fringe

pattern. If the phase of one beam changes with respect to the other, a shift in the fringe pattern occurs. Such a phase change is brought about by a change in refractive index along one beam path relative to the other. It can be shown that the fringe shift δ which occurs due to a change in plasma refractive index μ is given by

$$\delta = \frac{\Delta\phi}{2\pi} = \frac{L}{\lambda}\Delta(\mu-1) \qquad (2.3.2a).$$

Here L is the length of plasma traversed by a probing optical beam of wavelength λ, and $\Delta\phi$ is the corresponding shift in the phase difference between the two beams. The quantity, $\mu-1$, is known as the 'refractivity' of the plasma. If the fringe shift is relative to vacuum, then

$$\delta = \frac{L}{\lambda}(\mu-1) \qquad (2.3.2b).$$

One of the fundamental reasons for determining plasma refractive index or changes in it, is that from this information, plasma particle densities or variations in these can be evaluated. For most plasmas, excluding stellar interiors (Alpher and White, 1965), the relationship between plasma refractivity and particle number density is given by

$$\mu-1 = \sum_{\ell}(\mu_{\ell}-1) = \sum_{\ell} K_{\ell}N_{\ell} \qquad (2.3.2c),$$

where μ_{ℓ} is the refractive index of a particular species, ℓ (which could be one of electrons, positive ions, negative ions, ground- or excited-state atoms or molecules, etc.), N_{ℓ} is the number density of the species, ℓ, and K_{ℓ} is a constant called the 'particle refractivity', for the species, ℓ.

Two different types of interferometric measurement have been used in the present work, by which information has been gained relating to the behaviour of neutral gas molecules during the growth and decay of the low pressure and low current SF_6 spark. The first measurement involves the passage of both laser beams, whose phases are being compared, through the discharge. Fringe shifts obtained by this method yield information on gradients in refractive index (and hence in number density) between the paths followed by the two beams. The second type of measurement involves

sending one of the beams along an external path in which conditions remain fixed and well known throughout the experiment. In this way, absolute changes in phase difference between the beam probing the plasma (called the "scene" or "test" beam) and the external (or "reference") beam can be determined, from which absolute changes in plasma particle number density can be evaluated.

As already pointed out through equation 2.3.2c, each of the different species present in a discharge or plasma contribute to the net refractive index. It can be shown, however, that for the weakly ionized SF_6 discharges presently studied, the neutral species provide the greatest contribution to the refractive index, while the contribution due to the electrons is negligible (the latter will be proved in Section 3.2.4.(i)).

If the neutral molecules are the dominant species in the discharge, then to a good approximation, the plasma refractivity will be given by

$$\mu - 1 = \mu_g - 1 = K_g N_g \qquad (2.3.2d),$$

where g represents the neutral molecular species. For SF_6, the gas refractive index is 1.000783 (Schumb, 1947) at S.T.P., under which conditions N_g is simply given by the Loschmidt number. Consequently, K_g is evaluated to be 2.91×10^{-23} cm^3. For the present SF_6 discharges, equation 2.3.2a can be rewritten as

$$\delta = (2.91 \times 10^{-23}). \frac{L}{\lambda} \Delta N_g \qquad (2.3.2e),$$

where ΔN_g is in cm^{-3}. From this it is clear that for a particular minimum detectable fringe shift, the minimum possible variation that may be detected in SF_6 number density will vary inversely as the length L of the plasma traversed by a beam of fixed wavelength, λ. Hence if very low density plasmas are being studied, the length of the plasma traversed by the probing beam will need to be sufficiently long if small fractional changes in number density are to be detected. For this reason, a one-metre gap chamber (as already described in Section 2.1) has been constructed to allow adequate sensitivity in the interferometric study of 0.55 and 0.80 Torr SF_6 sparks.

For example, using the Lee-Woolsey polarization interferometer, (discussed in Section 2.3.2.(iii)) which measures to one-hundredth of a fringe, in the early stages of spark growth in 0.8 Torr SF_6 (again see Section 2.3.2.(iii)), the minimum detectable variation in gas number density is about $2 \times 10^{14} cm^{-3}$ for L = 1m and λ = 632.8 nm. This represents a variation of about 1% from the initial density.

The use of ring-electrodes which are flush with the wall of the metre-tube permits the unobstructed passage of the laser beam(s) through the plasma for radial positions from the axis to very close to the wall (since the beam diverges from 2.0 mm to 3.0 mm over the metre gap, its centre cannot be positioned closer than 1.5 mm from the wall at the entrance end if reflections are to be avoided).

To measure radial gradients in gas refractive index (and hence in gas number density) as a function of time during the low pressure SF_6 spark, a modified Jamin interferometer has been used. This experiment was motivated by the need to observe the extent of radial variations in the parameter E/N during spark development in the above gas. The interferometer arrangement and its properties will be described in Section 2.3.2.(ii), the results of the measurements obtained presented in Section 3.2.4.(ii), and an interpretation of these measurements given in Section 3.2.7.

In order to perform absolute refractive index (and density) measurements in SF_6 sparks in the metre-gap, it has been necessary to obtain an interferometer which is capable of (i) producing a sufficiently large separation between the scene- and reference-beams, so as to allow a clear path for the latter to follow outside the discharge tube, and (ii) providing a stable fringe pattern for a sufficiently long time even when the two ends of the interferometer are far apart and supported independently.

Unfortunately, however, no conventional interferometer exists which is capable of adequately satisfying both the above requirements simultaneously. Density variations in the transient SF_6 plasmas presently studied can occur over times as long as many tens of milliseconds, but conventional

interferometers are not suitable at these long times if the two ends are mounted separately and large beam shear is desired. For example, the classical Mach-Zehnder interferometer which comprises two semi-reflecting plates and two mirrors, has large beam shear capabilities, but is not stable for times of this order, if mounted in this manner. Under these conditions, the fringes are not visible to the naked eye unless the mountings are extremely stable. This instability can be attributed to the fact that the components on the separately mounted ends are reflecting-surfaces, which vibrate independently of one another (the vibrations could be due to a number of causes such as the operation of vacuum pumps and other motorized equipment in the vicinity, or simply due to ambient building vibrations). It is clear that even minute vibrations of these reflecting surfaces can induce a considerable deviation of the beams, over large distances.

One class of interferometer which is capable of providing a considerable degree of stability in the presence of vibrations is that which employs essentially refracting components and a minimum of reflecting parts. This is as would be expected, since for light rays incident on a glass plate, the refracted beam compared to the reflected beam would experience much less deviation when the plate is tilted.

Included in the above class, are polarization interferometers. Basically, these use a double refracting crystal such as a Wollaston prism to shear the incident beam into two separate components. These are then directed by a lens or mirror system toward a second identical double-refracting crystal by which they are recombined. The Smith polarization interferometer is one example (Françon, 1966). Despite the advantage of these interfermoeters over the Mach-Zehnder with regards stability, however, the lateral shear obtainable is limited by the size of the redirecting lens- or mirror-system used.

It might have been possible to use a Smith polarization interferometer on the present SF_6 discharge system by choosing lenses large enough to provide the lateral shear required ($\sim$ 36 mm minimum). However, a novel polarization interferometer designed by Lee and Woolsey (1981) which possesses the large shear and long beam path capabilities required for the examination of objects many times the size of the present SF_6 system, and which is stable even when the ends are separately mounted, has been used. This interferometer will be described in some detail in Section 2.3.2.(iii), the measurements made with it presented in Section 3.2.4.(iii) and the interpretation of the results given in Sections 3.2.5 to 3.2.7, inclusive.

2.3.2.(ii) The modified Jamin interferometer and recording system

In the conventional Jamin interferometer, an optically flat "parallel-sided" glass plate (with a wedge angle less than a few seconds of arc) is used to divide, by reflection at its front and back surfaces, an incident beam of monochromatic light into two parallel components. The separation between these component beams is limited by the plate thickness, so that for relatively thin plates both beams traverse the medium under study. At the output stage, these are recombined by another optically flat plate which is parallel to, and has the same dimensions as the first plate. A stable fringe pattern then results by very slightly tilting one plate with respect to the other. A shift in the fringe pattern will represent a change in the average refractive index gradient (and hence in average number density gradient) between the two beam paths.

In practice, few researchers now use this original form of Jamin interferometer since a much cheaper, whilst equally efficient version is available. This modified Jamin interferometer utilizes two wedge-shaped plates (with wedge angles of the order of 1 minute of arc) rather than parallel-sided plates. Woolsey and Illingworth (1972) successfully demonstrated the use of this version in the measurement of electron density gradients in an argon Z-pinch discharge.

The present experiment uses similar wedge-shaped plates to measure changes in gas refractivity gradient in the low pressure SF_6 spark. The optical arrangement is shown in Fig. 2.3.2.(i). A 1 mW helium-neon laser (Spectra Physics, Model 133) provides a 2 mm diameter beam of 632.8 nm radiation which is divided into two components by a *Vitreosil* glass plate, P_1. This plate has a thickness of 5.0 mm and its front and back surfaces polished to within one-quarter wavelength of sodium light. These surfaces are 30%- and 100%-reflecting, respectively. The two component beams pass through the metre chamber and recombine as shown at plate P_2, which is similar to P_1. The resultant fringe pattern is non-localized and can be viewed in any vertical plane outside P_2 and normal to the beams. With the aid of lens L, the fringe pattern is expanded and projected onto the plane of a narrow variable slit, S. This slit is directly attached by a flange arrangement to an EMI, type 9658A photomultiplier, and the P.M. output signal is fed to a Tektronix, type 551 oscilloscope. Hence, when the discharge is pulsed, variations in radial molecular density gradient cause the fringe pattern to move across the slit, thus producing changes in photomultiplier signal which can be observed on the oscilloscope.

The wedge angles of plates P_1 and P_2 have been calculated from a knowledge of the wavelength of radiation used, the plate refractive index and the fringe separation at the plates themselves. This fringe separation was accurately determined for both plates using Fizeau interferometry (Born and Wolf, 1975). For a plate refractive index of 1.46, wedge angles of 1.54×10^{-4} radians (0.54 minutes of arc) and 1.42×10^{-4} radians (0.49 minutes of arc) were obtained for plates P_1 and P_2 respectively.

The plates were mounted on commercial transverse saddles on separate optical benches clamped to the steel framework supporting the discharge tube, vacuum system and diffusion pump. The plates were adjusted in position so that the two beams were located 6 mm and 10 mm from the discharge tube axis. They were then oriented to give vertical fringes. It was found that the sharpest fringe contrast was obtained by minimizing the net wedge angle, i.e. by having

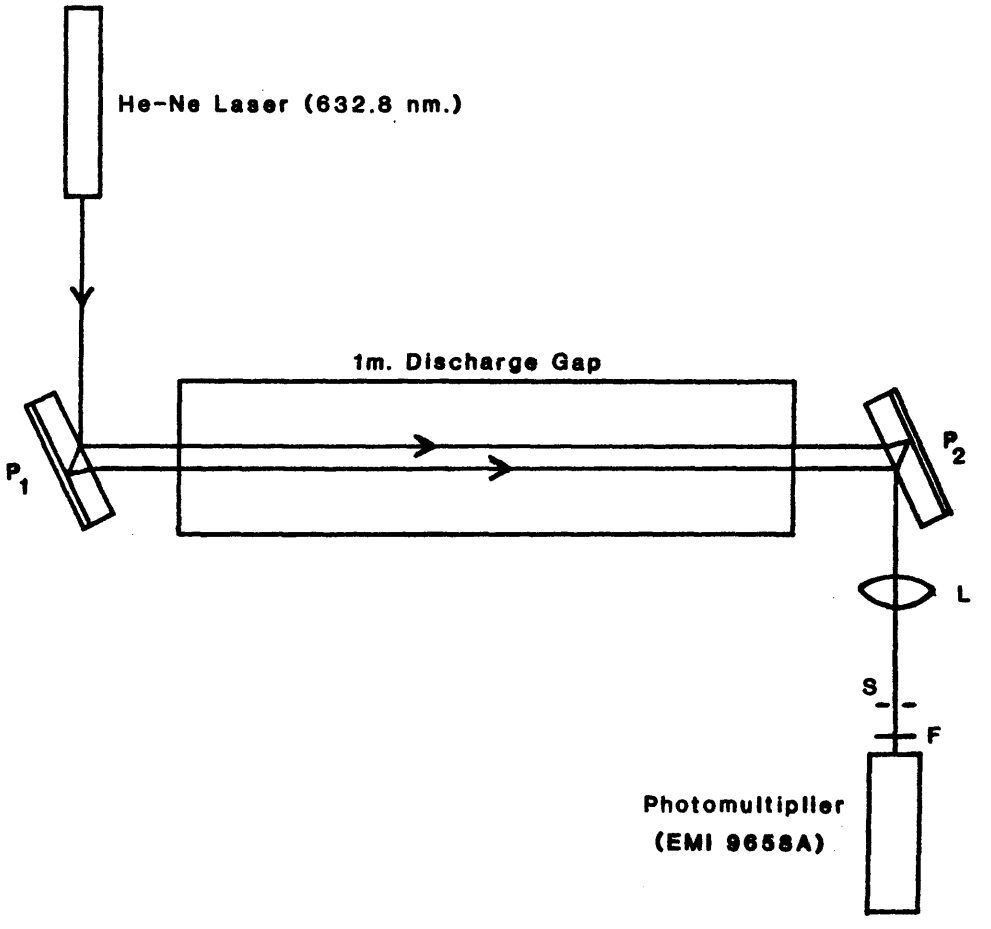

Fig. 2.3.2.(i) The modified Jamin interferometer system.

the wedges pointing in opposite directions (the location of the wedge on each plate was earlier found by observing on a distant screen the average separation of the multiple reflections for different plate orientations).

Due to the presence of the rotary pump and other motorised equipment nearby, the entire system was subject to considerable vibration. Despite this however, the fringe pattern obtained was stable. Woolsey and Illingworth attributed this to the fact that neither transverse nor longitudinal vibrations of plates P_1 and P_2 alter the difference in optical path traversed by the two beams of the interferometer. Rotational oscillations of the plates on the other hand can cause a displacement of the fringe pattern, but this is found to be a small effect.

For purposes of calibrating the photomultiplier traces obtained in the presence of the discharge plasma, it is necessary to know the photomultiplier signal amplitude corresponding to the difference in intensity between the middle of a bright and dark fringe. This information was obtained by inducing multiple fringe shifts through the rotational oscillation of plate P_2 using a small electric buzzer strapped to the plate mounting. At the same time, the width of the photomultiplier slit S, was optimized to obtain a maximum signal, so as to achieve maximum sensitivity (see Section 3.2.4.(ii)). A value of 0.5 volts was obtained for this peak-to-peak signal. The photomultiplier was then positioned so that the slit was in the middle of a dark fringe. This was done by moving the photomultiplier across the width of a chosen dark fringe on a transverse optical mount until a minimum d.c. light signal was detected.

When the discharge was initially pulsed, it was found that an appreciable light signal due to the discharge itself was obtained. To minimize this, a black cloth was used to cover the entire length of the metre-tube, and also a 10 $\mathring{A}$ band-filter designed to transmit the 632.8 nm line, was placed between the photomultiplier cathode and slit S. A negligible amount of light was then detected when the discharge was pulsed with the laser beam switched off.

Before proceeding with the experiment, a check was made on the extent of refractive deviation of the laser beams under the discharge conditions used. To do this, one of the interfering beams was blocked off so that the other beam could be viewed alone with the photomultiplier. The discharge chamber was then filled to a pressure of 0.55 Torr and pulsed at 10.0 kV. The intensity of the viewed beam remained constant throughout the duration of the spark. The same effect was observed when the other beam was monitored alone, thus indicating negligible deviation of the beams under the present discharge conditions.

2.3.2.(iii) The Lee-Woolsey polarization interferometer and recording system

The design of the Lee-Woolsey polarization interferometer referred to in Section 2.3.2.(i) was motivated by the need to make interferometric measurements on the present one-metre SF_6 discharge gap where it is necessary to have reasonable beam shear and fringe stability despite independent mounting of the input and output stages.

The interferometer consists of six identical rectangular block prisms and two half-wave plates. Each block is made up of a calcite prism which is cut parallel to the optical axis and which is cemented to an LF7 glass prism of the same angle. An LF7 glass plate is cemented to the plane calcite surface perpendicular to the optical axis. The block prism design is illustrated in Fig. 2.3.2.(ii). An incoming ray, normal to the first calcite surface produces an ordinary ray (o) and an extraordinary ray (e) at the calcite-glass interface. The rays are polarized at right angles to one another, and are deviated from the direction of the original beam by angles θ_o and θ_e respectively. The angular shear between the two rays is a function of the refractive index of the glass n_g and the prism angle ϕ. LF7 glass prisms have been used so that for a working wavelength of 632.8 nm in the present experiments, the angles θ_e and θ_o are equal. This comes about since the refractive index of LF7 glass is between the indices of calcite for the e- and o-rays at 632.8 nm. As pointed out by Lee and Woolsey, this symmetry

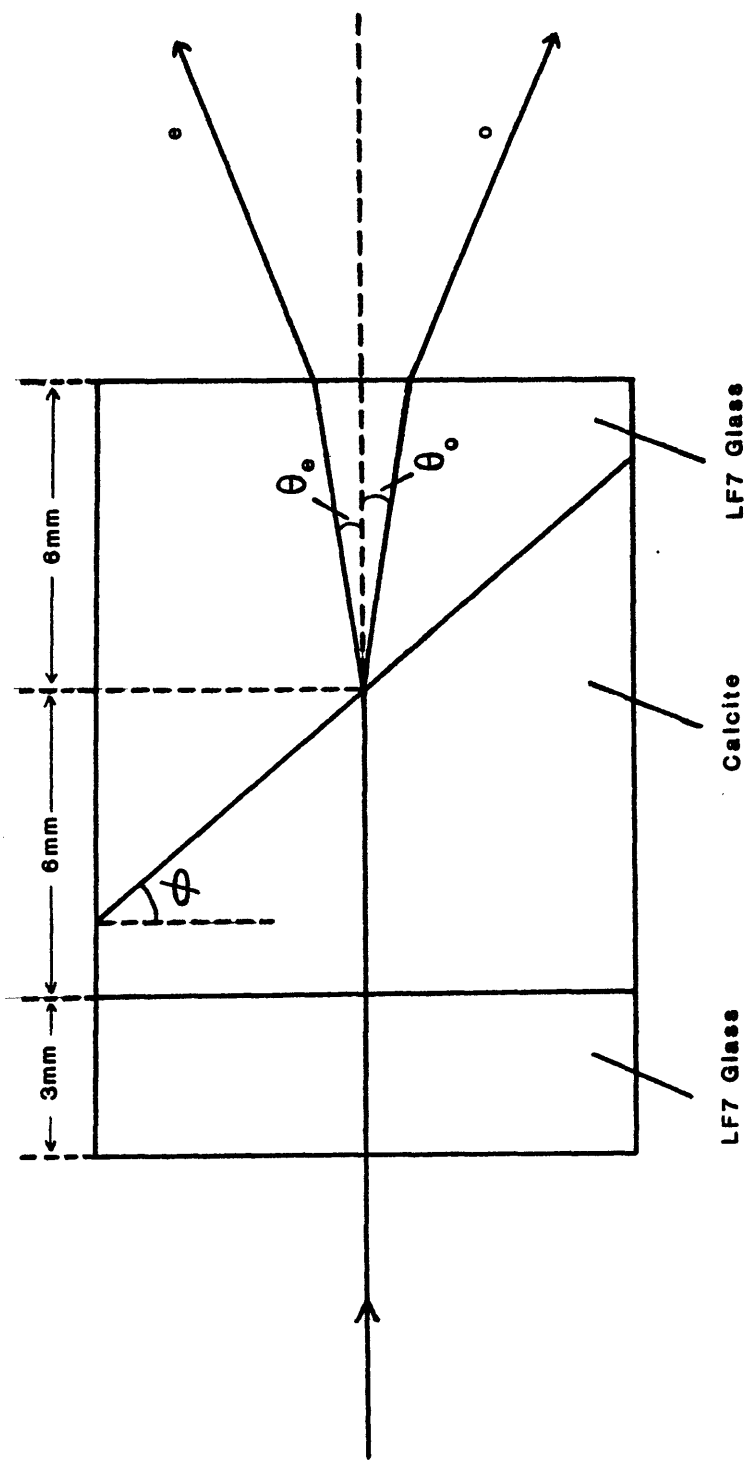

Fig. 2.3.2.(ii) The structure and dimensions of a rectangular calcite-glass block prism of the Lee-Woolsey polarization interferometer (after Lee and Woolsey, 1981).

of angle is not essential for the successful operation of the interferometer, but is convenient in many practical situations. The prisms were manufactured with angle ϕ of $39^0 52'$, giving an angular shear at the inclined calcite-glass interface of $5^0 12'$, and $8^0 10'$ at the final glass-air surface. This choice was a compromise between the amount of shear produced and the amount of calcite required to build each prism.

The LF7 glass end-plate is cemented to the plane calcite surface so as to protect that surface from external damage (calcite is somewhat softer than glass). The prisms thus have hard external refracting surfaces which can be readily polished and cleaned.

The interferometry assembly is shown in Fig. 2.3.2.(iii). Compared to a conventional polarization interferometer, the two pairs of prisms, $P_2(e)$ and $P_2(o)$, and $P_3(e)$ and $P_3(o)$ replace the lenses or mirrors. The first pair of prisms are reversed relative to the input prism P_1 and the second pair reversed relative to the output prism P_4. The original e- and o-rays produced by the first prism impinge upon the first pair of prisms, $P_2(e)$ and $P_2(o)$ and are refracted by them so that they are parallel to the direction of the initial beam. The half-wave plates W_e and W_o then act to reverse the polarizations of the two beams, so that when these beams pass through prisms $P_3(e)$ and $P_3(o)$ they are refracted toward each other and are recombined in the final prism P_4. The beam output from P_4 then passes through a polarizer which is oriented with its axis at 45^0 to the plane of polarization of both beams. This is necessary to rectify the two orthogonal vibrations into the same plane, so that they may interfere.

In the present work, a Spectra Physics, Model 138-02, 1 mW helium-neon laser is used to provide plane polarized radiation of wavelength 632.8 nm. The laser is oriented such that the plane of polarization lies at 45^0 to the optical axis of the calcite in the first prism. By doing this, the beam intensity is equally divided between the e- and o-rays.

The procedure adopted for prism alignment in the present experiments is relatively straightforward and is as given by Lee and Woolsey. This

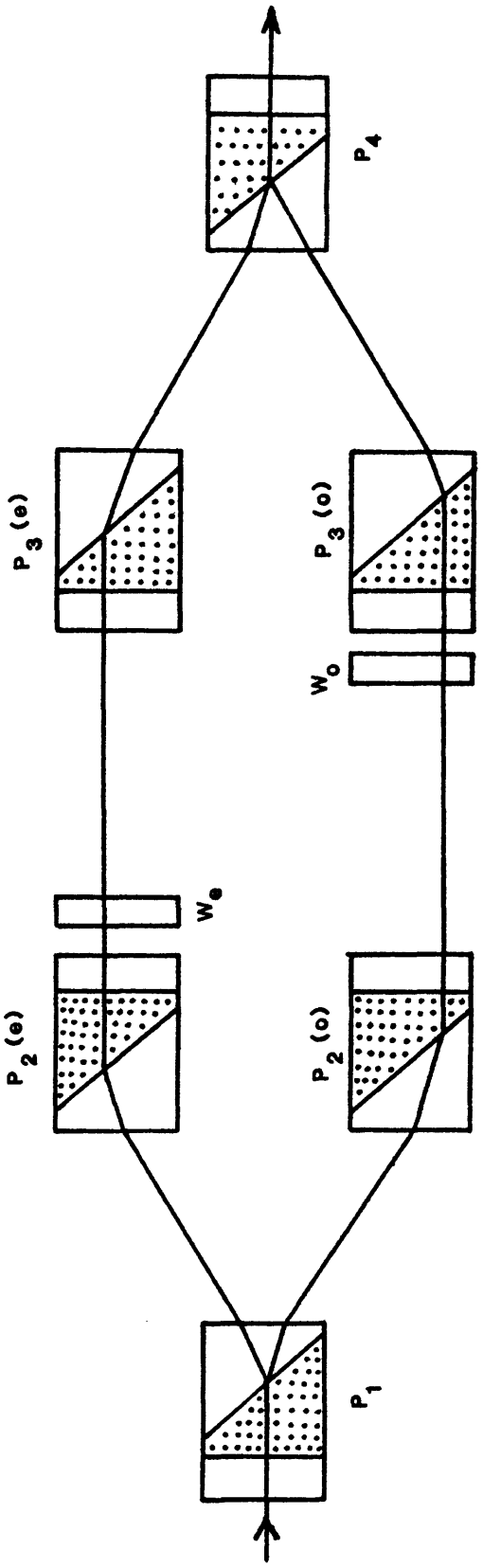

Fig. 2.3.2.(iii) The Lee-Woolsey polarization interferometer, consisting of six matching calcite-glass prisms and two half-wave plates (after Lee and Woolsey, 1981).

procedure will not be detailed here, but essentially it involves aligning the prism assembly such that the six calcite-glass interfaces are parallel, and adjusting the central prisms so that their centres are nearly equidistant from the interferometer axis (i.e. from that axis running through the centres of prisms P_1 and P_4). If the centres of the central prisms are set so they are exactly equidistant from this axis, then the two rays will have exactly equal optical paths through the system and a single infinitely wide fringe would be observed. Lee and Woolsey have shown that equal optical paths can be achieved over a wide range of input beam conditions. Thus the input beam can be incident upon the first face of prism P_1 at angles other than normal, and can even be off-axis, and the e- and o-rays will still have equal optical paths, provided the prism alignment conditions outlined above are met. For some prism arrangements in which the angled interfaces are set parallel, but where path symmetry does not exist (for example, in the case where the pair of central prisms on one side of the interferometer axis is not the same distance from it as that on the other), the optical path difference between the two beams remains constant for different incident angles and off-axis distances of the input beam. Interference between the two beams will therefore still be obtained, provided of course that some overlap occurs at the output surface. The flexibility of the input conditions means that not only is the overall alignment procedure made easier, but also that vibrations of the laser with respect to the input prism, P_1 are not critical.

With regard to the effect of vibrations, Lee and Woolsey have studied the various translations and rotations likely to affect the stability of the fringe pattern. They show that for any single prism, the only translation to have any significant effect on the fringe pattern is a horizontal movement normal to the beam in the plane of Fig. 2.3.2.(iii). For this translation of each prism, a complete fringe shift is incurred by a movement of the order of 10 μm. However, translational movements of up to 1 mm along the other orthogonal directions produce no visible change in the fringes. Rotations

of individual prisms about horizontal or vertical axes normal to the beam produce little fringe shift, approximately one milliradian being required to shift the pattern by a full fringe. However, the rotation of a prism about an axis along the beam direction has a significant effect, a single fringe shift being produced by a rotation of a few hundredths of a milliradian. Lee and Woolsey suggest that this particular rotation is unlikely to be excited in most practical situations. As for the half-wave plates, all translations are found to be unimportant. Rotations about any axis in the plane of the plate provide small changes in fringe pattern, but the rotations required are too large to be a stability problem. The authors suggest that rotations of the half-wave plates about the beam axes, large enough to affect fringe contrast, are unlikely to occur in practice.

In addition to the study of single-component vibrations, Lee and Woolsey have examined the stability of the fringes when separate sections of the interferometer are moved relative to one another. They considered three independent sections, the first comprising the laser, the second (or input section) made up of prisms P_1, $P_2(e)$ and $P_2(o)$ and half-wave plate, W_e, and the third (or output section) comprising prisms $P_3(e)$, $P_3(o)$ and P_4 and half-wave plate W_o. When keeping the laser and input sections fixed, it was found that the output section could be translated over several mm in any of the three cartesian directions without any noticeable disturbance of the fringe pattern. Further, rotations of the output section about a horizontal axis normal to the beams and about the beam axes themselves have a small effect. In contrast, however, rotation about a vertical axis of no more than 10^{-2} milliradians is found to cause a full fringe shift. The authors again suggest that such a rotation is unlikely to be excited, but if they are, precautions could be taken to reduce them to a negligible level.

In view of the vibrational motions which could affect fringe stability, special tables have been designed for use in the present experiments to house the input and output sections of the interferometer. These tables, which lie at either end of the metre-discharge tube, were made from welded

steel tubing and are adjustable in height by means of levelling screws on their bases. The transmission of mechanical vibrations from the laboratory floor to each table is reduced by placing small rubber pads of 8 mm thickness under each leg. Connected horizontally across the top of both tables are 13 mm mild steel plates of dimensions 1000 x 195 mm which are drilled and tapped on a 40 mm grid so that prisms and other components could be securely mounted onto them, in their desired positions. The plates are attached to Thompson ball bushes which run on stainless steel rods, mounted to the tables in a direction transverse to the discharge tube. This is done so that by rotating graduated dials connected to lead screws of 1 mm pitch, which attach the plates to the tables, the former can be smoothly moved transverse to the discharge tube. The rods and bushes have been chosen to minimize movement of the plates in every direction other than that transverse to the discharge tube. Before being attached to the plates, the prisms are housed in separate mounts. These mounts, which facilitate movement in all six degrees of freedom, were originally designed to investigate the role of different prism translations and rotations in the alignment of the interferometer. For the present experiment, this degree of movement is not essential for proper alignment, since as indicated earlier, the interferometer is relatively insensitive to some translations.

On the first table, is mounted the laser, together with the input trio of prisms and half-wave plate, W_e. This half-wave plate is mounted normal to the laser beam axis in a commercial lens positioner attached to prism $P_2(e)$. The prisms are adjusted to give a beam shear of 100 mm, and aligned so that by moving the first table transverse to the discharge tube, the scene beam could be swept across the horizontal diameter of the discharge tube. The three output prisms and half-wave plate, W_0 (the latter attached to the mount of prism $P_3(o)$) are then aligned with the polarizer and an expanding lens on the second table, and the fringes obtained projected onto a recording detector.

The stability of the system was found in general to be as predicted by Lee and Woolsey, although the presence of pump vibrations did affect the fringes to a small degree. Obviously, some of the more significant vibrations were not eliminated by the mounting system used. However, rather than trying to eliminate the vibrations by improving this system, it was found easier to perform all interferometric measurements with the vacuum pumps switched off. Under these conditions, the maximum fringe shift obtained from all sources other than the discharge itself (one of these being the oscilloscope, which incorporates a motor-driven fan) is 1/4 of a fringe in 50 ms. This represents the maximum accuracy to which the refractive index can be measured and compares favourably with the stability of conventional interferometers used in plasma studies (Blackwell, Cross and Falconer, 1979). The phenomena of primary interest in this interferometric study occur within the first 2 ms of discharge evolution, and so assuming the vibrations to have a linear effect, the results in this region will be accurate to $1/100^{th}$ of a fringe. As will be seen from typical interferograms (see Section 3.2.4.(iii)) this is also the maximum accuracy to which the traces can be analysed.

The recording system used to detect the fringes is a Hewlett-Packard, type HP5082-4205 photodiode with an effective collecting diameter of 1.5 mm. The detector and associated circuitry are mounted in a metal box, the light from the fringe pattern being collected by an aperture of 2 mm diameter. The signal produced by the detector is then fed to the Tektronix, type 551 oscilloscope via a 50Ω-coaxial cable.

The response time of the photodiode itself is of the order of nanoseconds, but the actual response time obtained is limited by its external circuitry. The risetime is estimated to be less than 10 μs. The slowness of this detector is not a disadvantage however, since the fastest density fluctuations observed occur in a time, a factor of 50 greater than this value (as verified using a photomultiplier detector).

Before using the Lee-Woolsey interferometer it was ensured (as was done before, using the Jamin) that negligible discharge light entered the detector, and that refractive bending of the scene beam was negligible under the operating conditions of the discharge.

CHAPTER 3

RESULTS AND DISCUSSION

3.1 SOME STUDIES RELATING TO PRE-BREAKDOWN AND BREAKDOWN IN THE LOW PRESSURE SF_6 SPARK

3.1.1 Control of the Statistical Time-Lag to Breakdown

3.1.1.(i) Control by cathode irradiation - An observation made regarding the operation of the U.V. lamp

The time interval to breakdown constitutes that period between the instant at which a voltage in excess of the static breakdown voltage is applied to the gap, and the instant at which this gap voltage begins to collapse due to current growth. This time-interval comprises the sum of the statistical and formative time-lags, as defined in Section 1.1. In the present studies the statistical time-lag is eliminated by illumination of the cathode surface with ultraviolet radiation from a Pen-Ray mercury lamp (described in Ch. 2), which has its most intense line at 253.7 nm. The lamp initially was operated continuously. It was found however, that when using the 1-metre discharge chamber, the statistical time-lag could be eliminated even with the U.V. lamp switched off, provided that the lamp was located in a position close to the highly stressed cathode. It was found that a statistical time-lag was only obtained when the U.V. lamp was physically removed from the cathode vicinity. From these and other observations, it was inferred that the quiescent U.V. lamp was being activated within nanoseconds of gap-voltage application, to produce photoelectrons from the cathode. When using the 1-metre discharge chamber, statistical time-lags have been eliminated using this mode of lamp operation in preference to that of continuous irradiation, since the use of the quiescent mode eliminates the need to provide eye protection against continuous U.V. irradiation. It is of interest to examine the mechanism responsible for lamp activation in its quiescent state. Initially, it was supposed that r.f. radiation from the CX1140 thyratron may have excited the lamp. To test whether it was possible to excite the U.V. lamp with this radiation, a variable air-spark-gap was used in place of the thyratron in the circuit of Fig. 2.2.1, since such a gap provides strong emission of r.f. radiation and would allow for

easier detection of lamp excitation. The spark gap was first adjusted to break down at 8 kV, and the discharge gap evacuated to less than 1 micron, so that it could not break down. Under these conditions, when the storage capacitor was charged to +8 kV, the spark gap was observed to pulse sporadically as it was not able to maintain conduction. Every time a spark-gap pulse occurred, the quiescent U.V. lamp which was located near the discharge cathode (cf. Fig. 2.2.1), was visually observed to "flash". However, when the U.V. lamp was subsequently placed adjacent to the pulsing spark gap and away from the cathode, no flashes were seen. The latter observation suggested that it was unlikely that r.f. radiation from the thyratron was responsible for exciting the U.V. source under the experimental conditions. The flashing of the lamp each time the spark gap discharged, was shown to be associated with the switching of the capacitor voltage across the discharge gap. A high negative d.c. voltage was applied to the discharge cathode, with the anode grounded. It was observed that when the U.V. lamp was brought close to the cathode, it flashed, and further, when it was withdrawn from the cathode region, it flashed again. The same effect was observed if the lamp was located in its operating position close to the cathode and the applied negative voltage was raised or lowered. On the other hand, if a high positive voltage was applied to the anode with the cathode grounded, no flashing occurred. These observations suggest that when the lamp, which has a dual-bore fused silica tube, of length 5.4 cm and bore-diameter, 1.5 mm, is subjected to an external electric field, polarization of the quartz walls occurs. As illustrated in Fig. 3.1.1.(i), the charges on the inner wall can produce large enough electric fields to break down the mercury vapour within the bore. Diffusion of electrons and positive ions from the resultant discharge to the wall rapidly reduces the field produced by polarization and the discharge goes out. When the external electric field is removed however, the polarization effect is removed, and the wall-charges remaining from the previous discharge provide a field which produces a further pulsed discharge.

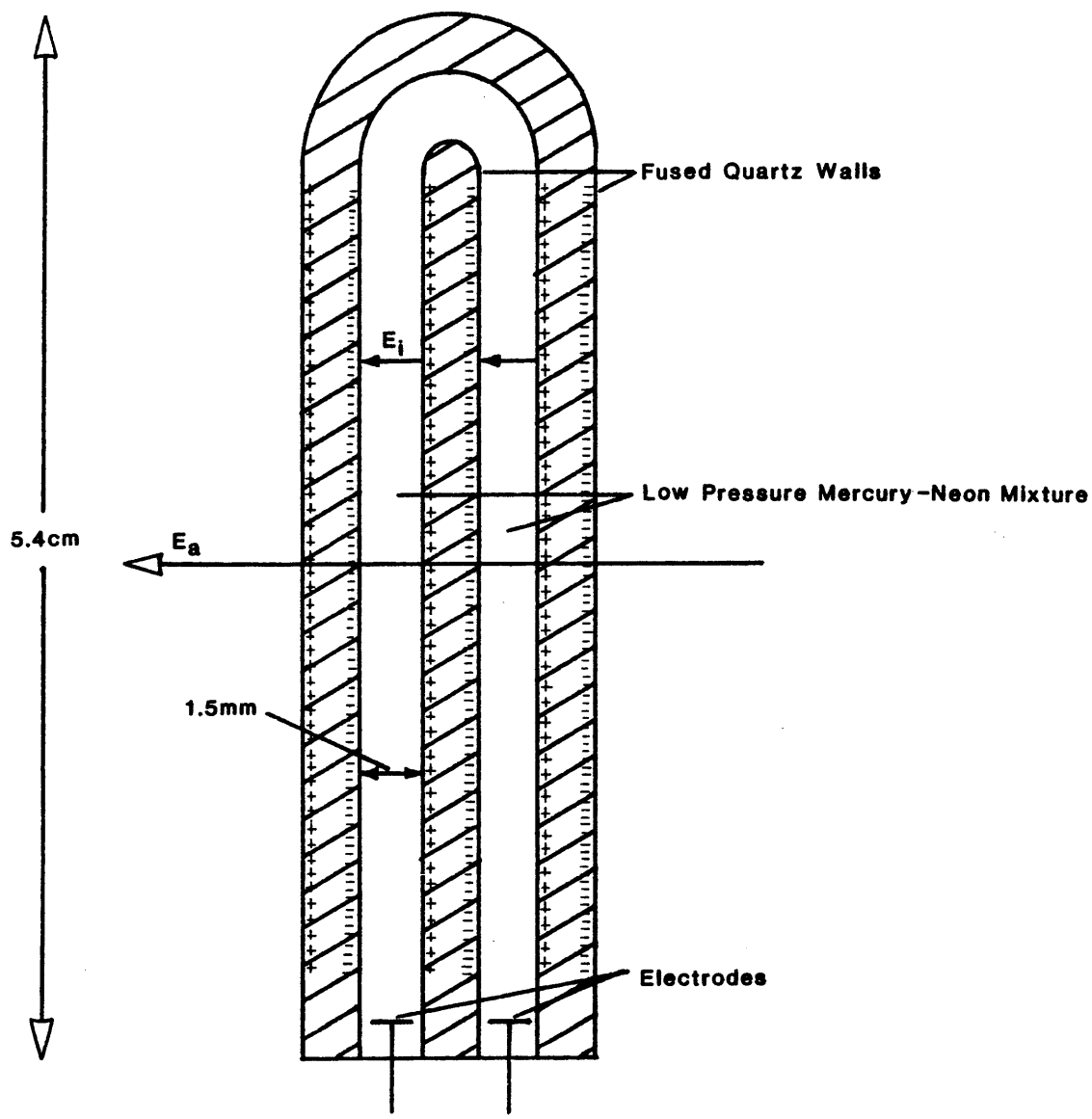

Fig. 3.1.1.(i) A schematic diagram of the mercury-neon Pen-Ray (Model, 11SC-1) U.V. lamp showing the electric field (E_i) induced within the lamp bore by wall polarization, when the lamp is subjected to an external electric field, E_a.

Whenever the U.V. lamp was used with the small, movable-electrode chamber, it was necessary to operate the lamp in a continuous mode in order to eliminate the statistical time-lags. Only relatively low voltages (up to 3 kV) were switched across this chamber and the resultant electric fields developed across the U.V. lamp were not large enough to discharge the lamp.

3.1.1.(ii) Control by irradiation of a section of the gap away from the cathode

It has been found possible to exercise some control over the statistical time-lag in SF_6, by irradiating, with ultraviolet light, the discharge gap rather than the cathode surface. Lewis (1975) has reported a reduction in the statistical time-lag for an iodine vapour discharge, as a result of gap irradiation. Working at overvoltages in excess of 250%, a gas pressure of 0.24 Torr and a gap length of about 8 cm, Lewis attributed this effect to a combination of the following gas processes: (a) dissociative attachment of electrons to I_2 molecules and (b) the photodetachment of I^- ions by the applied U.V. irradiation. It was postulated that during the comparatively long time-interval between successive discharge shots (the apparatus used was operated under single-shot conditions), a number of electrons produced within the gap by cosmic rays would become attached to form I^- ions. With gap irradiation, photodetachment of these ions would provide a source of electrons to initiate avalanche growth when an appropriate electric field is applied. The photodetachment cross-section of I^- is high at 253.7 nm which, as in the present studies, was one of the most intense lines of the radiation used. On the basis of this hypothesis, it is surmised that a similar effect might also occur in SF_6. The time-interval to breakdown, both with and without the irradiation of a section of the discharge gap, was observed for the 1-metre discharge chamber by observing the applied voltage pulse. A small part of the mid-gap zone of the metre chamber was irradiated to ensure that no reflections from the tube walls could reach the cathode surface. An SF_6 pressure o 50 mTorr and an applied gap voltage of 6 kV were used. Under conditions of

continuous mid-gap irradiation, thirty successive shots were fired, with a fresh SF_6 fill admitted after every ten shots. It was observed that for five of the thirty shots, the discharge gap failed to break down, while for the other twenty-five, a mean statistical time-lag of 310 ± 65 μs was obtained, using the von Laue-Zuber analysis (Meek and Craggs, Ch. 7., 1978). In this analysis, a statistical distribution of time-lags superimposed on a formative time-lag (t_f) is described by

$$\frac{N_t}{N_o} = \exp\left[\frac{(t_f - t)}{\bar{t}_s}\right] \qquad (3.1.1a)$$

where N_o = the total number of time-lags recorded, N_t = the number which occurred for times greater than t, and $\bar{t}_s$ = the mean statistical time-lag. The plot of $\ln\left[\frac{N_t}{N_o}\right]$ against t should yield therefore, a straight line with gradient $\left[-1/\bar{t}_s\right]$ which intercepts the time-axis at t_f. The plot thus obtained for the condition of continuous gap-irradiation is shown in Fig. 3.1.1.(ii). Also shown in this figure is a plot obtained for the same conditions of pressure and applied voltage, without gap irradiation. In this case too, thirty shots were fired, with a fresh SF_6 fill being admitted to the chamber after every ten shots. It was found that for twelve of the applied shots, the discharge failed to break down. The application of the von Laue-Zuber analysis to the remaining eighteen breakdowns, gave a mean statistical time-lag of 1.3 ± 0.3 ms. The formative time-lags cannot be properly resolved on the plots, but have been observed to be less than 1 μs under conditions of cathode-irradiation, for the same pressure and applied voltage. It can be seen that although the percentage uncertainties in the two mean statistical time-lags are large (given by $\frac{100}{\sqrt{N_o}}$ %, where N_o is the total number of breakdowns observed, a reduction of about 75% in $\bar{t}_s$ is obtained when the mid-gap zone in SF_6 is irradiated. No such effect was observed however, when argon was used under the same conditions. A further investigation has shown that under conditions of gap irradiation, the mean statistical time-lag in SF_6 is dependent on the applied E/N-value (E being the applied field and N the gas number density). Measurements were made of $\bar{t}_s$ under conditions of mid-gap

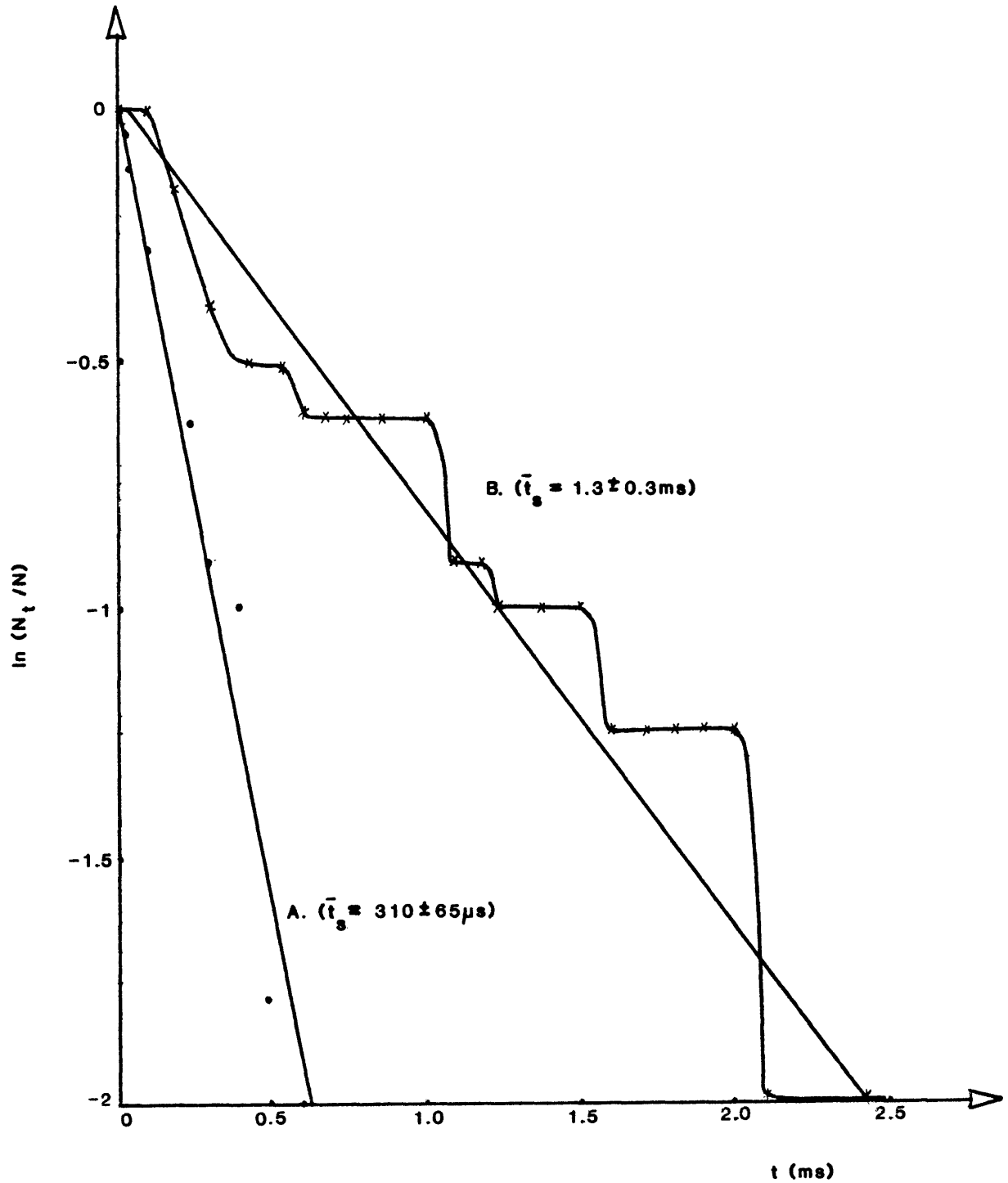

Fig. 3.1.1.(ii) von Laue-Zuber plots obtained for a 50 mTorr SF_6 spark, pulsed in the metre-gap at 7 kV, for conditions of continuous mid-gap irradiation (curve A) and for no U.V. irradiation (curve B). The corresponding mean statistical time lags are shown.

irradiation for SF_6 filling pressures of 15, 60 and 250 mTorr, using an applied voltage of 8 kV in each case. A total of twenty breakdowns was observed at each pressure, and it was found that although the percentage uncertainty is large (± 23%) a definite increase occurs in $\bar{t}_s$ with pressure. Fig. 3.1.1.(iii) illustrates the decrease in $\bar{t}_s$ with increase in applied E/N.

The reduction in the mean statistical time-lag produced by continuous gap-irradiation, can be accounted for by processes similar to those described for iodine. During the quiescent state, low energy electrons produced within the gap by cosmic rays will attach to SF_6 through the resonance-capture processes 1.3.3d and 1.3.3e (see Section 1.3.3.(ii)). Upon irradiation, the resultant negative ions may be photodetached:

$$SF_5^- + h\nu \longrightarrow SF_5 + e \qquad (3.1.1b)$$

$$SF_6^- + h\nu' \longrightarrow SF_6 + e \qquad (3.1.1c).$$

Although the photodetachment cross-sections for these negative ions are still not well established, the above processes could reasonably be expected to occur, since sufficient energy appears to be available from the radiation used. It was shown in Section 1.3.3.(iii) that the upper-limits to the vertical detachment energies of SF_6^- and SF_5^- are 4.53 eV and 4.9 eV respectively. It is likely however, that the detachment energies of these ions are considerably lower than the upper limits quoted, especially if there exist stable excited electronic states of SF_6^- and SF_5^- from which detachment could occur. Fehsenfeld (1970) has suggested that such states will exist for SF_6^-. The 253.7 nm mercury resonance line, is one of the most intense lines irradiating the gap, and has an energy equivalent to 4.9 eV. Consequently, photodetachment from both SF_6^- and SF_5^- is possible. Hence if electrons are photodetached at or around the instant of voltage application to the gap, then the mean statistical time-lag could be expected to be smaller, as observed. It is not surprising that the mean time-interval to breakdown decreases with an increase in the applied E/N, since the photodetached electrons will have

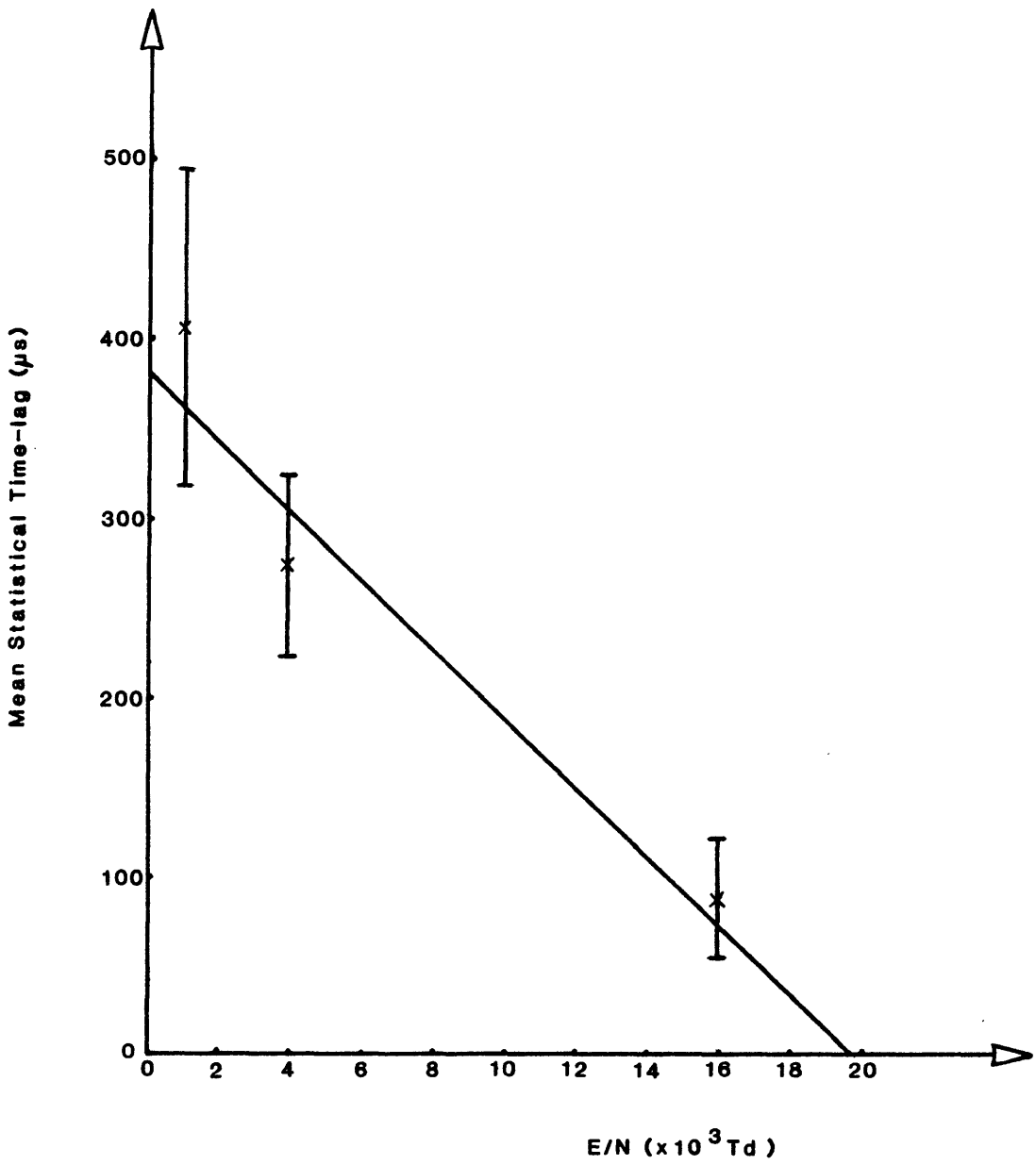

Fig. 3.1.1.(iii) A graph of the mean statistical time-lag as a function of applied E/N under conditions of continuous mid-gap irradiation of the metre-chamber.

less chance of becoming re-attached to the SF_6 molecules at higher values of E/N (refer to Section 1.3.3.(ii)), and are therefore more likely to be successful in initiating the breakdown process.

3.1.2 Breakdown-Voltage Measurements

The static breakdown voltage (V_s) for both the metre-chamber and the movable-electrode chamber, was determined as a function of Nd (N = gas number density and d = gap length). These data for the two non-uniform field configurations allow percentage overvoltage values to be quoted for different experimental conditions. The circuitry used for the measurements consisted of a stabilized d.c. power supply (Brandenburg, Model 800), a 10 MΩ limiting resistor and a microammeter of full-scale deflection 250 μA, all connected in series with the discharge tube. The voltage across the gap was measured using a 1000:1 voltage divider (Fluke, Model 80K-40) and a digital voltmeter accurate to 0.1%. The procedure adopted in the measurements was to slowly raise the applied voltages until breakdown occurred at a particular value of Nd, as evidenced by the sudden collapse of the gap voltage and the simultaneous production of a self-maintained current of the order of 100 μA. The voltage across the gap at which the sudden current increase was initiated, was taken as the static breakdown voltage, V_s. For both tubes, this breakdown voltage was checked several times for a particular Nd-value, with a fresh fill of SF_6 being used each time. The scatter from shot-to-shot in V_s for any particular set of conditions always remained within 100 volts. Fig. 3.1.2.(i) illustrates the breakdown voltages thus obtained for the two gaps as a function of reduced electrode separation (Nd) in the range $2.5 \times 10^{17}\ cm^{-2} < Nd \leqslant 3.3 \times 10^{18}\ cm^{-2}$. The uniform-field Paschen curve for SF_6 in the range $5 \times 10^{16}\ cm^{-2} \leqslant Nd \leqslant 4.86 \times 10^{18}\ cm^{-2}$ has been included for comparison. The data points of the latter curve have been taken from a table published by Dakin *et al.* (1974) - see Meek and Craggs, Ch. 6, (1978). Measurements of V_s in the metre-tube were made over the pressure range $0.1\ Torr \leqslant p \leqslant 2\ Torr$, while measurements in the variable-electrode chamber

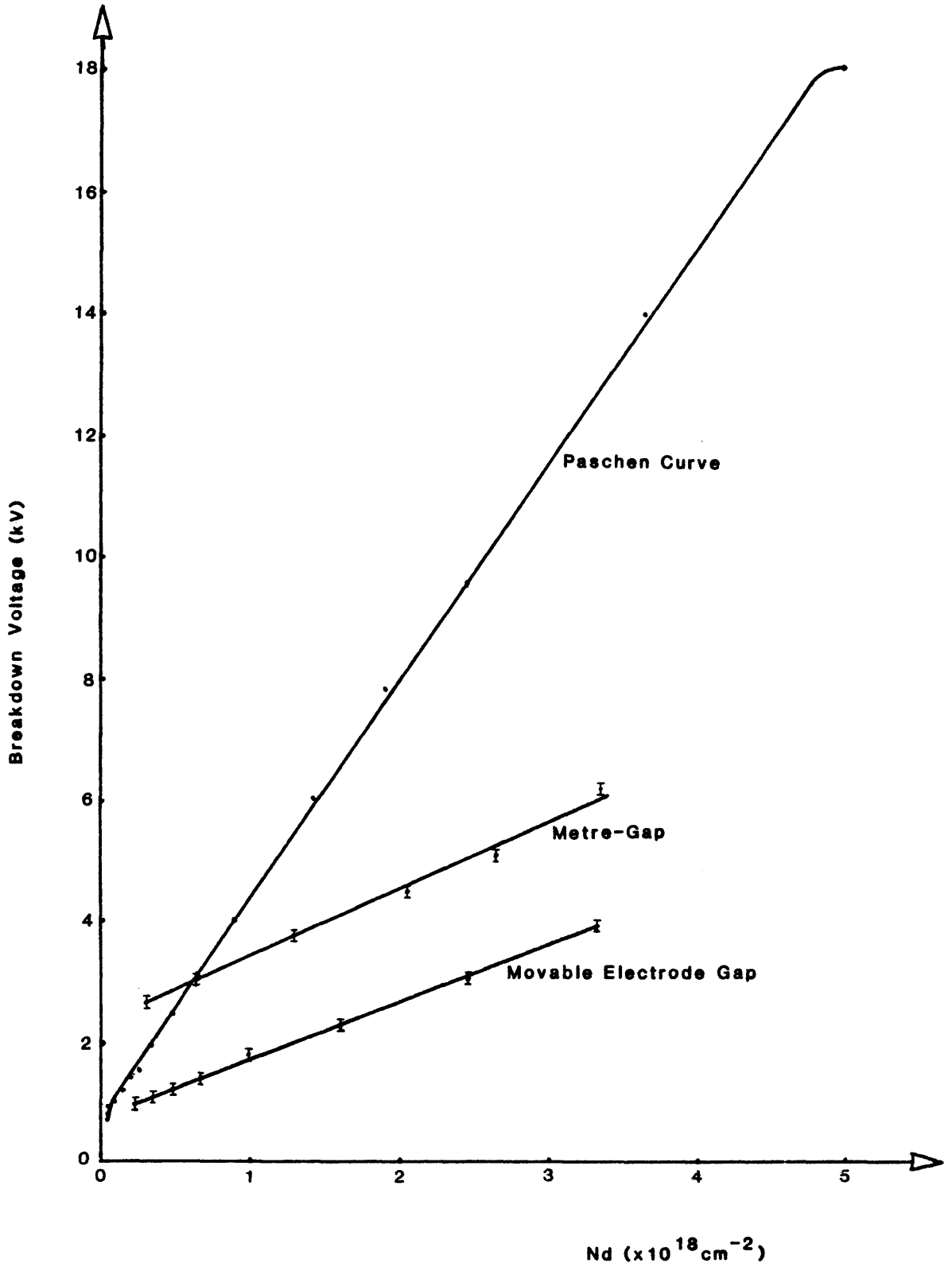

Fig. 3.1.2.(i) Breakdown voltage curves for SF_6 in the metre-gap and the movable-electrode gap in the range 2.5×10^{17} cm^{-2} $\leqslant$ Nd $\leqslant$ 3.3×10^{18} cm^{-2}. Included for comparison is the Paschen curve for SF_6 in the range 5×10^{16} cm^{-2} $\leqslant$ Nd $\leqslant$ 4.86×10^{18} cm^{-2} (the latter curve is after Dakin *et al.*, 1974 - see Meek and Craggs, 1978).

were made at different pressures and gap-lengths in the ranges 1.5 Torr $\leqslant$ p $\leqslant$ 5 Torr and 8 cm $\leqslant$ d $\leqslant$ 20 cm, respectively.

The applied percentage overvoltage (ΔV) for a particular value of Nd can thus be obtained from equation 1.1a. Very high percentage overvoltages have been used in the present experiments in order to produce sparks which pass through all the post-breakdown phases catalogued in Section 3.2.2. For example, in the case of a 0.80 Torr SF_6 spark pulsed in the metre-gap, the minimum overvoltage required to take the spark into the so-called "dissociated glow phase" (see Section 3.2.2) was approximately 100%. At overvoltages below this, only the first current pulse (as shown for example in Fig. 3.2.2.(iv)) was obtained followed by a decaying low current phase before the spark extinguished.

It is worth pointing out that the effect of electrode microprotrusions on the breakdown voltage in the present low pressure studies, will be negligible. The effect of surface roughness on breakdown voltages has been discussed in Section 1.3.3.(v)b. Observation of Crichton *et al.*'s (1976) curve of roughness factor, ξ versus pR (refer to Section 1.3.3.(v)b for the definitions), shows that for pure SF_6, $\xi = 1$ for pR $\leqslant$ 50 bar μm. From electron microscope pictures of the plane electrodes used in the small discharge chamber, it has been estimated that the height of any observed "protrusions" was no greater than 5 μm. Hence for a pressure of 2.5 Torr, pR = 3.3×10^{-3} bar μm. (The use of the protrusion height only, as the characteristic dimension is adequate, and has been used by Farish (1982) in describing similar roughness-factor curves for SF_6 and SF_6 mixtures.)

3.2 POST-BREAKDOWN DEVELOPMENT IN LOW PRESSURE SF_6 SPARKS

3.2.1 Introduction

The SF_6 spark presently studied has been produced in the two discharge chambers described in Ch. 2 using the electrical circuitries described therein, at pressures between 0.5 Torr and 3 Torr. The SF_6 spark, which evolves through a number of distinct post-breakdown phases and transitions before gap recovery occurs, has been studied using the various time-resolved techniques described in Section 2.3. This study has been complemented by an oscillographic study of sparks in argon/SF_6 mixtures and by the study of low pressure, low current d.c. discharges in SF_6. These d.c. discharges have properties similar to those of certain phases of the spark discharge.

The aim of the present chapter is to describe the phases and transitions of the low pressure SF_6 spark and some phenomena associated with them. Description of each of the phases requires constant reference to the time-resolved measurements made with the diagnostic apparatus described in Section 2.3. The format of presentation adopted therefore, is to first present all the time-resolved measurements and the assumptions made in obtaining them, without making any interpretations. The individual phases will then be presented with a discussion and interpretation of the time-resolved measurements, including where relevant, a discussion of the argon/SF_6 measurements and those made in the d.c. SF_6 discharge. One exception to this format has been made with regard to the measurement of cathode-fall potentials in the SF_6 spark. In this case, it is more convenient to discuss the measurements and interpretation simultaneously.

The first of the time-resolved measurements involves an oscillographic study of the spark current, i(t) and voltage, V(t) as functions of applied voltage, gas pressure, gap length and electrode configuration. In Section 3.2.2 a classification of the various spark phases and transitions is presented, followed by a description of the dependence of the amplitude and duration of the various phases on the above discharge parameters.

The second group of time-resolved measurements involves the determination of the axial electric field, E for different stages of discharge evolution. This has been done using the variable-gap, plane-electrode chamber described in Ch. 2. Both the method and the measurements will be presented in Section 3.2.3. Although the electric fields in the metre-gap could not be measured directly, useful estimates can be made from a knowledge of the voltage distributions in the small gap.

In Section 3.2.4 the time-resolved laser interferometric measurements of absolute gas refractivity and refractivity gradient will be presented. As already explained in Section 2.3.2, these measurements, which are made in the metre-gap using the Lee-Woolsey and modified Jamin interferometers, yield information on particle number densities (N) and density gradients $\left[\frac{\Delta N}{\Delta r}\right]$ in the spark. It will be shown in Section 3.2.4 that the electrons and particle species other than the ground-state SF_6 molecules, contribute negligibly to the total plasma refractivity. It turns out that the measurements of N are only valid for the early stages of discharge growth, i.e. up till time t_D, since thermal dissociation is known to become significant after this time. Obviously, species other than the neutral SF_6 molecules will then also contribute appreciably to the total plasma refractivity. The transition to the thermal dissociation phase will be discussed in Section 3.2.7.

From a knowledge of the axial field, E(t) and gas density, N(t), the reduced field parameter, $\frac{E}{N}(t)$ can be estimated at least for the early phases.

Having presented measurements on the parameters i(t), V(t), E(t) and gas refractivity as a function of time, the individual phases and transitions will be discussed in Sections 3.2.5 to 3.2.9.

3.2.2 Oscillographic Current and Voltage Measurements

Figure 3.2.2.(i) shows the complete temporal development of the current and voltage in the low pressure SF_6 spark prior to gap recovery. This oscillogram represents the development of a 3.0 Torr SF_6 spark pulsed at 3.0 kV in the small chamber of gap-length 4.0 cm. The pulsing circuitry used

Fig. 3.2.2.(i) Oscillogram showing the current trace (upper) and voltage trace (lower) for a 3.0 Torr SF_6 spark pulsed in a 4.0 cm gap at an applied gap voltage of 3.0 kV and at an overvoltage of 150%.

Gap Voltage (kV)

0 −1 −2 −3

2 1 0

Current (A)

Time (2μs/div.)

here was as described in Section 2.2.1. The cathode unit used comprised a 1 cm diameter stainless-steel disc surrounded by a machinable ceramic disc, as described in Section 2.1.

Figure 3.2.2.(ii) is a schematic diagram of the current profile displayed in Fig. 3.2.2.(i), categorizing the discharge phases and transitions which occur during spark growth. These include, (i) the time-interval up to and including breakdown, t_0-t_A, certain aspects of which have already been discussed in Section 3.1.2, (ii) the 'space-charge' phase spanning the time interval, t_A to t_B, (iii) the 'electronegative glow' phase from t_B to t_D, (iv) the 'dissociated glow' phase from t_D to t_E, (v) the glow-to-arc transition t_E to t_F and (vi) the arc phase which exists from t_F onwards until the charged capacitor is no longer able to maintain this phase.

The arc phase has not been obtained in the metre gap despite the high applied percentage overvoltages (such as 120% in the case of a 0.8 Torr spark pulsed at 12.00 kV), due partly to the large series resistor used (6.6 kΩ: see Fig. 2.2.1). In the case of the small tube, it was found that for a particular set of experimental conditions, it was easier to generate the arc phase using the cathode configuration described above rather than by using the larger 'all-metal' plane cathode. The reasons for this will be discussed in Section 3.2.9.

Interest in the present work on low pressure SF_6 sparks, has centred on the electronegative glow phase and the transition to the dissociated glow phase.

When using the small discharge chamber in the study of the early phases specified above, the 'all-metal' plane electrodes were used, and the applied overvoltages reduced so as to avoid generating the arc phase. This was done mainly so that evacuation of the chamber between consecutive discharge shots would be less time-consuming (if the arc phase occurred, longer evacuation times would be required due to the increased out-gassing of the electrode surfaces). Most of the oscillograms displayed therefore only include the phases up to (and sometimes including) the dissociated glow. Oscillograms

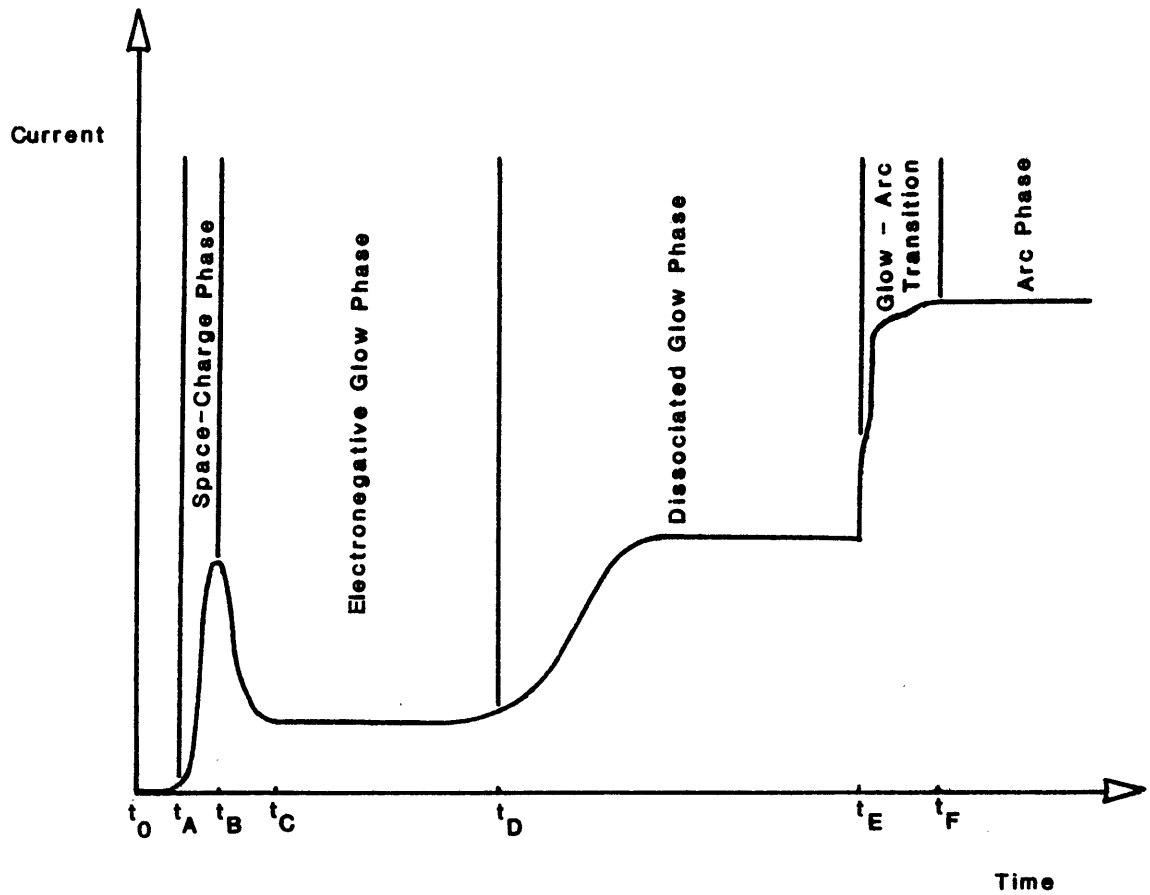

Fig. 3.2.2.(ii) A schematic diagram showing post-breakdown current growth in the low pressure SF_6 spark. The various quasistable phases and transitions are shown, together with the relevant time intervals.

Fig. 3.2.2.(iii) Oscillograms showing the current traces (upper) and voltage traces (lower) for a 1.5 Torr SF_6 spark pulsed in a 9 cm gap at voltages of 3.0 kV, 2.75 kV and 2.50 kV, and at overvoltages of 140%, 120% and 100%, respectively.

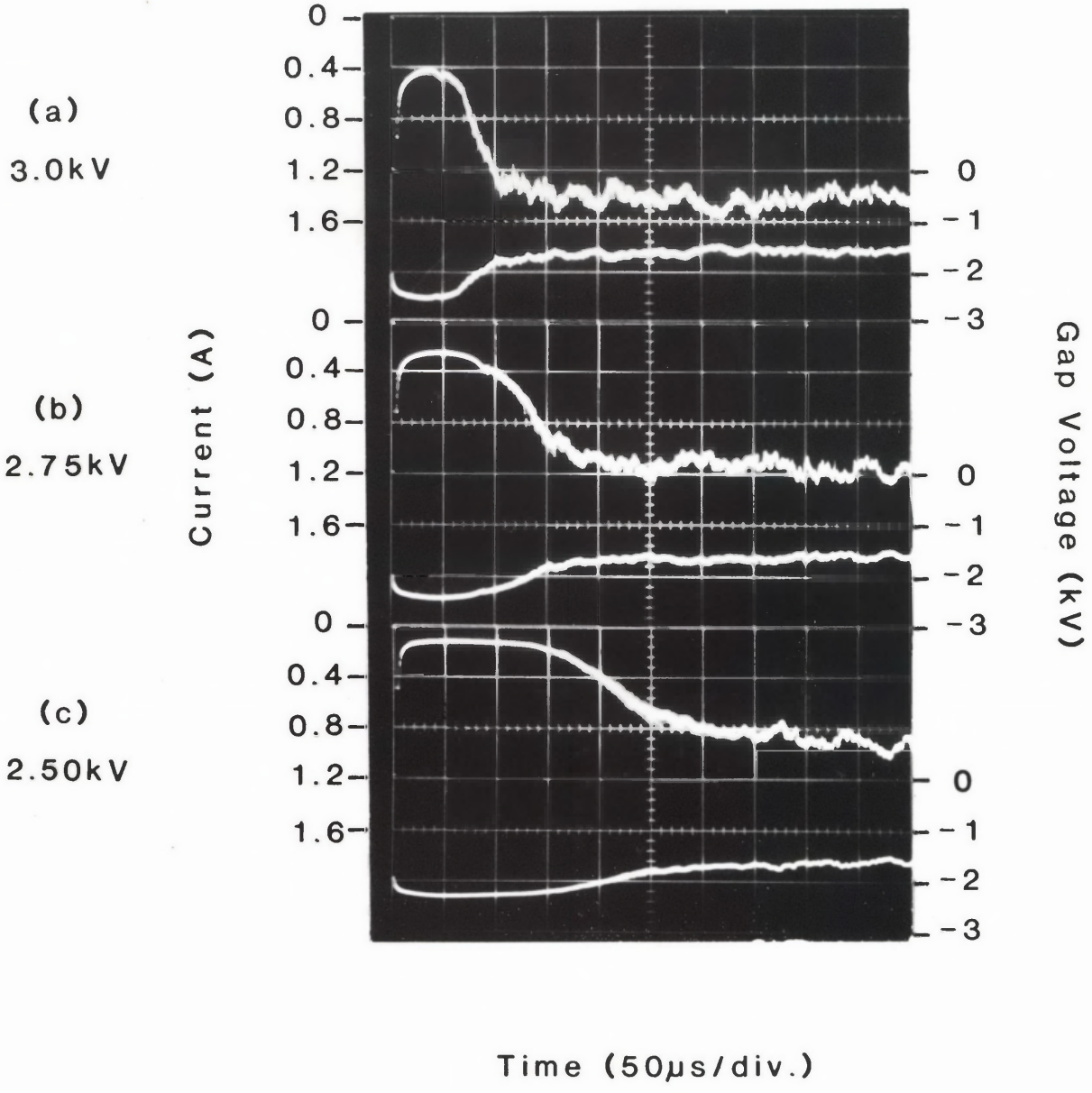
(a)
3.0kV
(b)
2.75kV
(c)
2.50kV
Current (A)
0
0.4
0.8
1.2
1.6
Gap Voltage (kV)
0
-1
-2
-3
Time (50μs/div.)

Fig. 3.2.2.(iv) Oscillograms showing current traces (upper) and voltage traces (lower) for a 0.80 Torr SF_6 spark pulsed in the metre-gap at applied gap voltages of 12.00 kV, 12.50 kV and 13.00 kV, and at overvoltages of 120%, 129% and 138%, respectively.

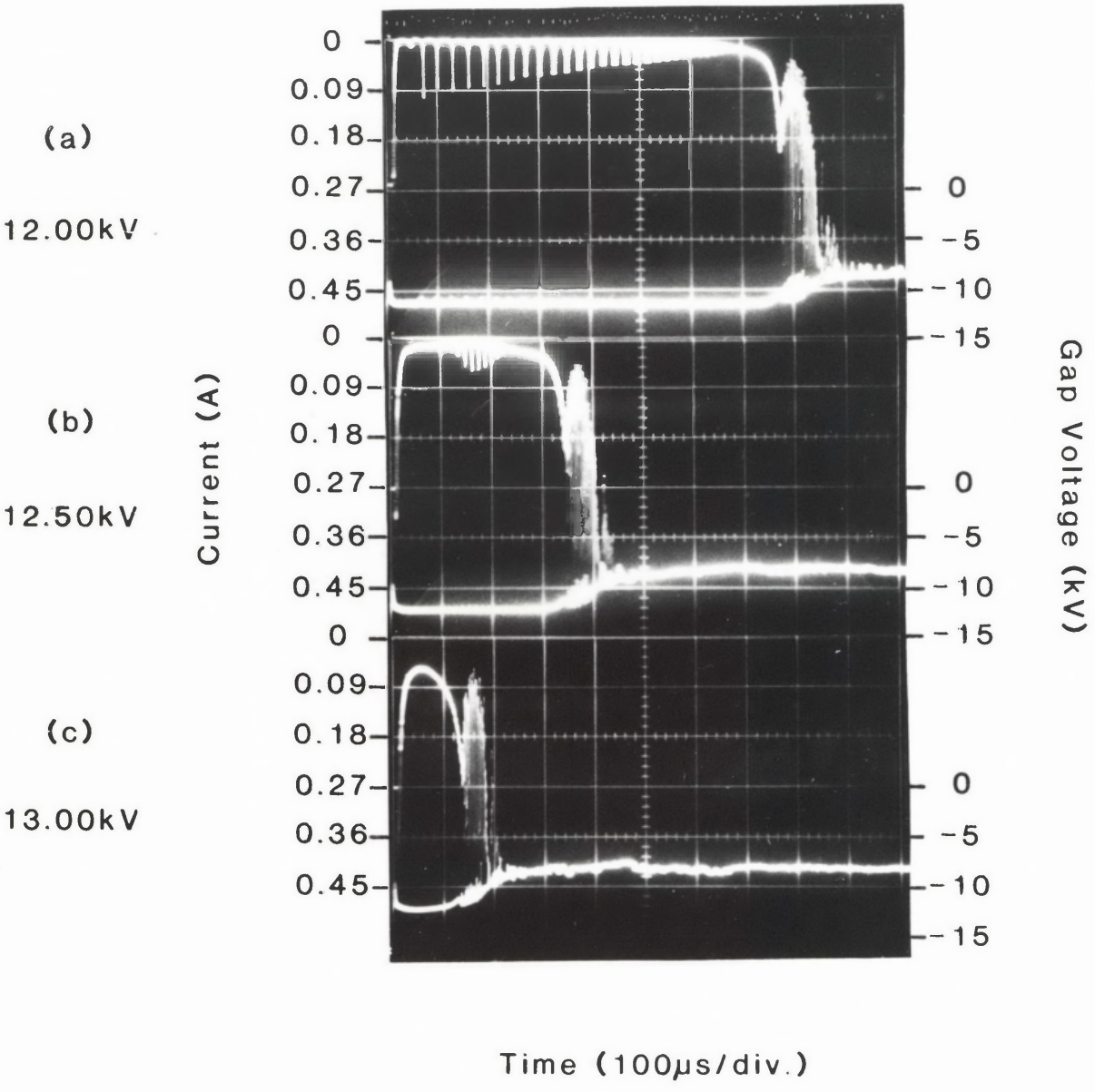
(a)
12.00kV
(b)
12.50kV
(c)
13.00kV
Current (A)
0
0.09
0.18
0.27
0.36
0.45
Gap Voltage (kV)
0
-5
-10
-15
Time (100μs/div.)

a, b and c of both Fig. 3.2.2.(iii) and Fig. 3.2.2.(iv), show typical current and voltage traces for these phases as obtained for different discharge conditions in the two chambers. The three oscillograms of Fig. 3.2.2.(iii) refer to a 1.5 Torr SF_6 spark pulsed in a 9 cm gap at applied voltages of 3.0 kV, 2.75 kV and 2.50 kV (and hence at percentage overvoltages of approximately 140%, 120% and 100% respectively, as evaluated from the appropriate breakdown curve of Fig. 3.1.2.(i)). The total series resistance used in this case was 1165Ω. The corresponding oscillograms of Fig. 3.2.2.(iv) refer to a 0.8 Torr SF_6 spark pulsed in the metre-gap at applied voltages of 12.00 kV, 12.50 kV and 13.00 kV (which correspond to percentage overvoltages of 120%, 129% and 138% respectively). From these figures the variations in duration and amplitude of the phases with applied voltage, can be observed. When the applied voltage is held constant and either the pressure p or gap-length d increased, the duration and amplitude of each phase is found to follow the same trend as shown in these figures when the applied voltage is reduced. The current pulse phenomenon observed in the electronegative glow phase of Fig. 3.2.2.(iv) constitutes a separate study and will be discussed in Section 3.2.6.II.

3.2.3 Post-Breakdown Axial Field Measurements

As indicated in Section 1.1, the electric field configuration in a spark gap changes rapidly from the applied-field configuration due to the establishment of space-charge regions during the immediate post-breakdown phase. Measurement has been made of the axial electric field distribution in the SF_6 spark for specific times following time t_A.

A procedure commonly adopted in determining the axial potential distribution in d.c. glow discharges consists of measuring the total gap voltage for various electrode separations. The method requires that the discharge current be maintained constant for all electrode separations, in order that the axial potential distribution remains constant. It is generally accepted that the cathode- and anode-falls in potential remain independent of electrode

separation (Francis, 1956). Various investigators have employed this method in determining axial fields in spark discharges (e.g. Cavenor and Meyer, 1969; Lewis and Woolsey, 1981). Here the discharge current at one particular time during spark development is adjusted to the same value at each electrode separation, by applying to the spark gap a voltage pulse of appropriate magnitude. This procedure is then repeated for other times so that variations in axial field as a function of time can be determined.

In the present work, this method has been used to obtain axial voltage distributions for three different times during the evolution of the SF_6 spark at 1.6 Torr in the movable electrode chamber. The method has proved reliable from the point of view of the excellent reproducibility of oscillographic traces from shot-to-shot. This was always the case for any particular set of pressure and gap-length, provided a fresh fill of gas was admitted before each shot. This reproducibility is demonstrated in the oscillograms of Fig. 3.2.3.(i) which represent current and voltage development in the 1.6 Torr spark pulsed in a 10 cm gap at 3.02 kV. The total series resistance used in this case was 139$7\Omega$. Referring to this figure and to the schematic diagram of Fig. 3.2.2.(ii), the three chosen times were (i) $t = t_B$, corresponding to the peak of the space-charge phase, (ii) $t = t_o + 100$ μs, which is in the electronegative glow phase and (iii) $t = t_o + 300$ μs, which is in the dissociated glow phase. The currents at these particular times were adjusted at each electrode separation to within 20 mA of the values displayed in Fig. 3.2.3.(i), i.e. to 310 mA, 53 mA and 320 mA. It was found that this procedure could be carried out quite accurately, although for the shortest gap-lengths used (6 cm and 7 cm) it was difficult to set the current in either of the two glow phases to the above values at the chosen times, without beginning to appreciably alter the relative positions on the current and voltage waveforms corresponding to these times. Thus for example, whilst in the 10 cm gap, time $t = t_o + 300$ μs corresponds approximately to the start of the steady-current part of the dissociated glow phase (see Fig. 3.2.3.(i)), for a 6 cm gap it corresponds to a time 80 μs after the establishment of this steady current phase. A similar,

Fig. 3.2.3.(i) Oscillograms showing current traces (upper) and voltage traces (lower) for three separate 1.6 Torr SF_6 sparks pulsed in a 10 cm gap at 3.02 kV and at an overvoltage of 130%.

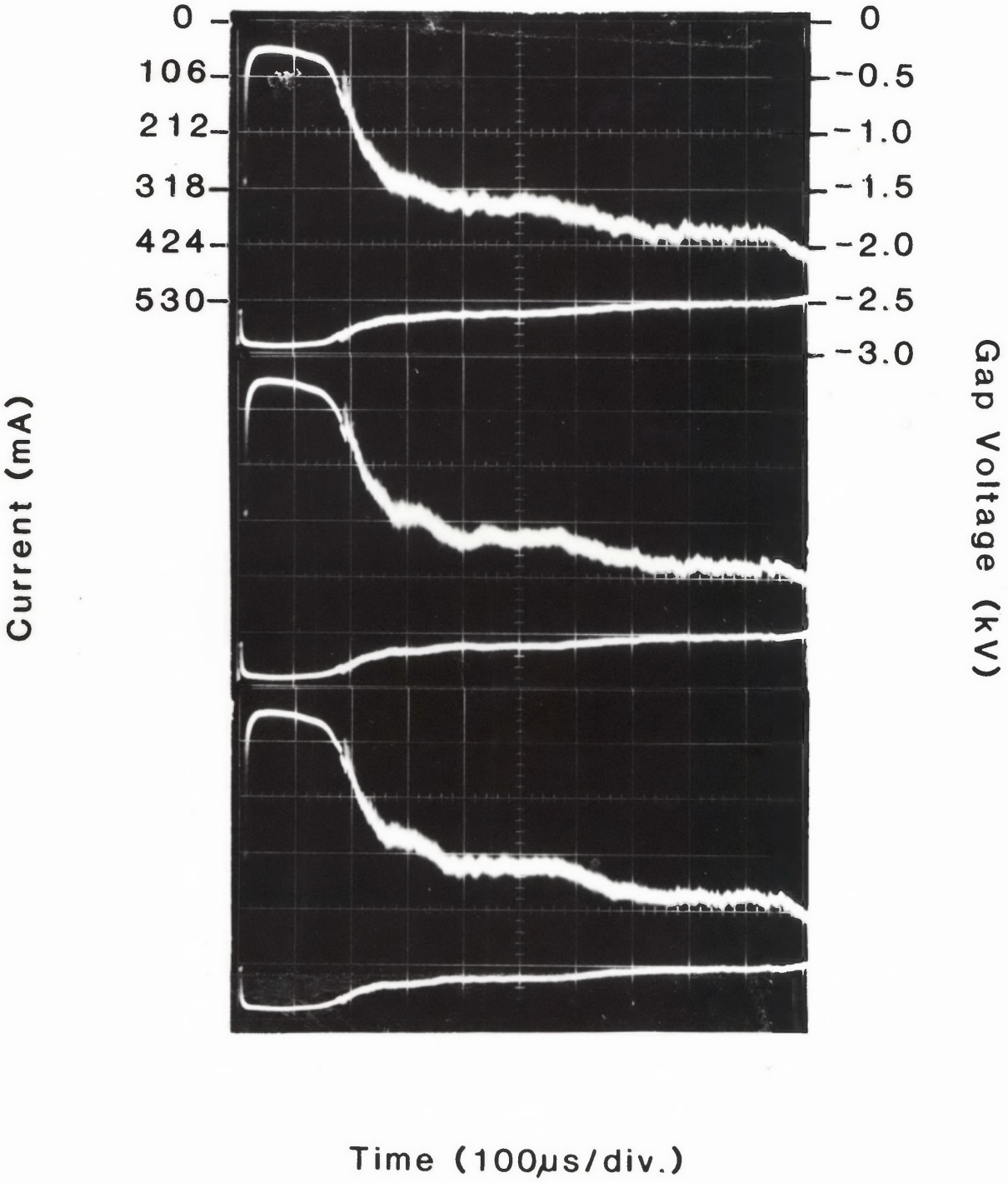
0
106
212
318
424
530
Current (mA)
0
-0.5
-1.0
-1.5
-2.0
-2.5
-3.0
Gap Voltage (kV)
Time (100μs/div.)

although less appreciable effect, occurs when setting the current for time $t = t_o + 100$ μs in the smaller gaps. Fortunately, however, this effect is of little consequence so long as the absolute chosen time always remains within the same phase, since measurements have shown that there is negligible variation in the axial field distribution during either of the glow phases. The distributions obtained for the three specified times are as shown in Fig. 3.2.3.(ii). The applied field distribution at time t_o is not known since the gap configuration is not uniform. Nevertheless, it could be assumed that if field distortions near the electrodes are not significant, then the applied field in the 10 cm gap would be of the order of 300 Vcm^{-1}. In the immediate post-breakdown phase, the axial field collapses from the applied value due to space-charge build-up near the electrodes as indicated earlier. At time t_B, the measured axial (positive column) - potential distribution is linear and equal to (120 ± 25) Vcm^{-1}, while at $t = t_o + 100$ μs the field has apparently increased to (168 ± 25) Vcm^{-1} and decreased at time $t = t_o + 300$ μs to (125 ± 30) Vcm^{-1}. Further discussion of these axial fields will be presented when dealing with the individual phases.

The extrapolation of measured potential distribution to zero electrode separation yields a voltage drop comprising the sum of the cathode- and anode-falls in potential, provided that the cathode dark-space, negative glow, Faraday dark-space and anode glow are thin (∿ mm). This will be the case in electronegative gases such as SF_6, at a pressure of 1.6 Torr (see Emeleus and Sayers, 1938; Cobine, 1941). In ordinary electropositive gases, the anode fall is of the order of the ionization potential of the gas (Cobine, 1941), which is less than 20 volts in the case of most monatomic gases. This is small in comparison with the cathode fall (which is hundreds of volts for most gases using metal electrodes) and it can thus be taken that the 'zero-length' voltage drop represents the cathode fall to within a few per cent. In electronegative gases, the anode fall is likely to be higher than in other gases because of the existence of a fairly well established negative-ion space-charge sheath near the anode surface. However, it has been shown

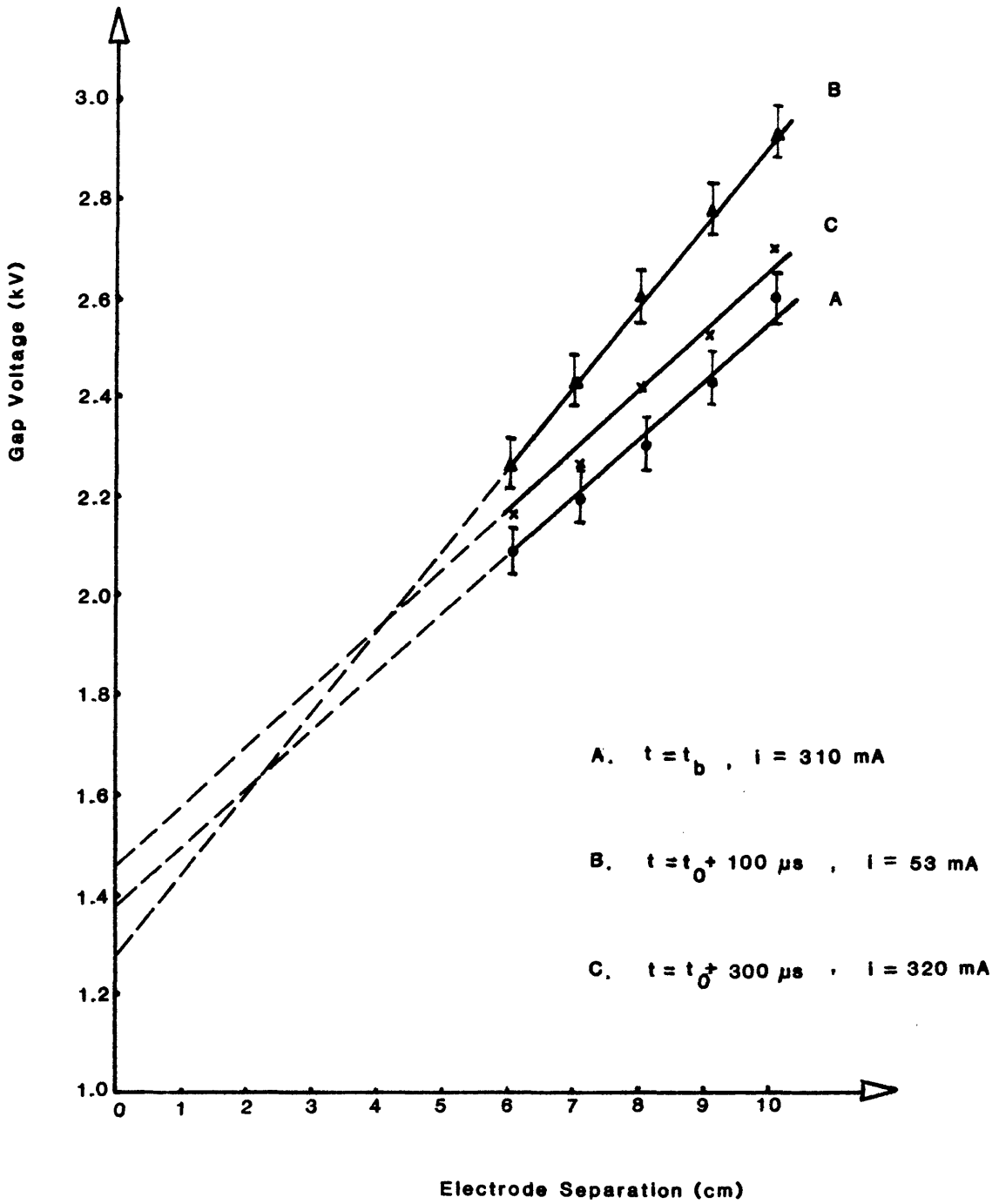

Fig. 3.2.3.(ii) Axial potential distributions at three different times during discharge evolution in a 1.6 Torr SF_6 spark. Times $t = t_o + 100$ μs and $t = t_o + 300$ μs referred to in the key, are in the electronegative and dissociated glow phases, respectively (see the oscillograms of Fig. 3.2.3.(i)).

(Woolsey, 1963) that the anode fall in a d.c. iodine discharge at 0.2 Torr and 2.5 mA is no greater than 10% of the corresponding cathode fall. Using this fact as an approximate guide therefore, it may be assumed that in the present work the 'zero-length' voltage represents the cathode fall to within about 10%.

The cathode fall at all three times is high, being approximately (1350 ± 125) V, (1250 ± 150) V and (1400 ± 150) V at times t_B, $t = t_o + 100$ μs and $t = t_o + 300$ μs, respectively. The combination of large cathode fall and low current suggests that the SF_6 spark discharge is an abnormal glow at these times. This view is supported by observations made of d.c. SF_6 discharges at similar pressures and currents, which reveal that the cathode surface is always completely covered by the cathode glow (indicating its abnormal nature). Similar observations were made by Emeleus and Woolsey (1970) in low current d.c. discharges in iodine. Further, Lewis and Woolsey (1981), studying the low current phase of a 0.36 Torr iodine spark discharge, reported cathode fall values in excess of 2400 volts and concluded that this phase represented an abnormal glow.

The abnormal nature of low-current SF_6- and iodine-glows is probably due to the high rates of electron attachment in the glow phase. Under these conditions an abnormally high cathode fall voltage would be required to maintain conduction.

3.2.4 Interferometric Measurements of Gas Refractivity and Radial Refractivity Gradients in the SF_6 Discharge

3.2.4.(i) Introduction: Contribution of electrons and species other than ground state SF_6 to the plasma refractivity

As indicated in Section 2.3.2.(i), every species present in a discharge or plasma will contribute to the net refractive index μ, by equation 2.3.2c. In high current plasmas, the electronic contribution is by far the most important. Under these conditions, the plasma refractivity (μ-1) can be approximated (see Alpher and White, 1965) by

$$\mu - 1 \doteqdot \left[\frac{-\omega_p^2}{2\omega^2}\right] \qquad (3.2.4a),$$

where ω is the frequency of the probing wave and ω_p is the electron plasma frequency, given by

$$\omega_p = \left[\frac{N_e e^2}{\varepsilon_0 m_e}\right]^{\frac{1}{2}} \qquad (3.2.4b).$$

Here e, m_e and N_e are the electronic charge, mass and number density, respectively and ε_0 is the permittivity of free space.

A calculation of N_e will thus allow an estimate to be made of the electronic contribution to the net plasma refractivity.

Interferometric measurements have presently been made with the modified Jamin interferometer (described in Section 2.3.2.(ii))on a 0.55 Torr SF_6 spark pulsed at 10.00 kV in the metre-gap and with the Lee-Woolsey interferometer (described in Section 2.3.2.(iii)) on a 0.80 Torr SF_6 spark pulsed at 12.00 kV in the same gap. The oscillograms of Figures 3.2.4.(i) and 3.2.4.(iii) show the interferometric traces obtained, with their corresponding current waveforms. From an analysis of the current waveforms for these sparks, the electron number densities can be determined, thus allowing the electronic contribution to the plasma refractivity to be evaluated. Consider for example, the 0.8 Torr, 12 kV spark. The current trace of this discharge shows the net ionization development from breakdown to a time 50 ms later when the gas has returned to its insulating state. To evaluate the maximum possible electron concentration, let it be assumed that the entire discharge current of the dissociated glow phase (of magnitude 0.7A, as seen from the current trace) flows through a constricted core of radius 2 mm. This is not an unreasonable assumption since low pressure d.c. glow discharges in SF_6 running at similar currents as in the present sparks are constricted to a channel of about this radius. Now, the maximum possible electric field in the column (neglecting the cathode fall) is 120 Vcm^{-1}. Assuming for the present, that the gas number density N in the core can be approximated by the initial number density of 2.64×10^{16} cm^{-3} (corresponding to a pressure of 0.80 Torr at 293 K), then

the maximum E/N is 454 Td. At this E/N the electron drift velocity v is 2.7×10^7 cm s^{-1}, as seen from the results of Kline *et al.* (1979) in Fig. 1.3.3.(iii). The maximum possible electron number density can now be calculated from the equation,

$$(N_e)_{max} = \frac{J_{max}}{ev} = \frac{i_{max}}{Aev} \qquad (3.2.4c)$$

where J is the current density, A the discharge cross-sectional area, i the discharge current and e the electronic charge. On substitution (i_{max} = 0.7 A, radius = 2 mm and v as above), $(N_e)_{max}$ is 1.3×10^{12} cm^{-3}. From equations 3.2.4a and 3.2.4b therefore, the maximum possible electron refractivity can be calculated. Consequently, from equation 2.3.2b, the maximum fringe shift relative to vacuum caused by an electron concentration of 1.3×10^{12} cm^{-3} in a one-metre length of plasma which is traversed by a probing wave of wavelength 632.8 nm, is found to be

$$\delta_{max} = 3.8 \times 10^{-4} \qquad (3.2.4d).$$

As indicated earlier, and will be seen in Section 3.2.4.(iii), the maximum sensitivity with which the Lee-Woolsey interferometer traces can be analysed is one-hundredth of a fringe, thus making the calculated electronic contribution to the plasma refractivity of the 0.8 Torr, 12 kV spark entirely negligible.

Other species which could contribute to the total refractivity of the SF_6 discharge apart from the ground state SF_6 molecules are the negative ions, positive ions and excited neutrals. To calculate the 'particle-refractivities' of these species (i.e. of the constant K_ℓ for each species ℓ, as in equation 2.3.2c), the so-called Slater screening-constant method is generally used (Alpher and White, 1959).

For the present discharges however, where the degree of ionization and excitation is generally low, it could be expected that if the positive and negative ions and excited neutrals have particle refractivities of a similar order of magnitude as that of the ground-state neutrals (which, generally is the case, except for certain electronically excited species for which K could

exceed the value for the ground-state molecules, by a factor of 100 (Alpher and White, 1965)), then their contributions to the total plasma refractivity will be small and so can be neglected. On this basis, it is taken that only the ground-state molecules contribute to the total discharge refractivity.

3.2.4.(ii) The modified Jamin interferometer measurements

The modified Jamin interferometer was set up as described in Section 2.3.2.(ii) with its glass plates oriented such that the beams were located 6 mm and 10 mm from the tube axis. Figure 3.2.4.(i) shows the resulting current and interferometric traces (upper and lower traces, respectively) obtained for the discharge conditions already specified in Section 3.2.4.(i).

In order to analyse the interferometric trace of Fig. 3.2.4.(i) in terms of fringe shifts, account has to be taken of the fact that the intensity distribution of the fringe pattern producing the trace is of a $(\text{cosine})^2$ form given by

$$I = 4I_0 \cos^2 \left(\frac{\phi}{2}\right) \qquad (3.2.4e)$$

where ϕ is the phase difference between the two beams, each of intensity I_0 at the point of interference (Born and Wolf, 1975). Taking the photomultiplier signal amplitude at time t_o to be zero (since as explained in Section 2.3.2.(ii) the photomultiplier slit is located in the middle of a dark fringe before firing the discharge), the amplitude, y, of any part of the interferometer trace can be given by

$$y = (0.5) \cos^2 \left(\frac{\phi}{2}\right) \qquad (3.2.4f)$$

where the maximum photomultiplier signal amplitude of 0.5 volts is equivalent to the maximum intensity of a bright fringe ($4I_0$). Hence it can be shown that if the photomultiplier slit is sitting in the middle of a dark fringe prior to the discharge being fired, then the fractional fringe shift δ corresponding to a particular point on the trace of amplitude y is given by

$$\delta = \frac{\Delta\phi}{2\pi} = \left[\frac{1}{\pi} \cos^{-1} \left\{\frac{y}{0.5}\right\}^{\frac{1}{2}} - \frac{1}{2}\right] \qquad (3.2.4g).$$

Fig. 3.2.4.(i) Oscillogram showing the current trace (upper) and Jamin interferometer trace (lower) for a 0.55 Torr SF_6 spark pulsed in the metre-gap at 10.00 kV and at an overvoltage of 127%.
The interferometer trace is obtained with the Jamin laser beams located 6 mm and 10 mm off the discharge tube axis.

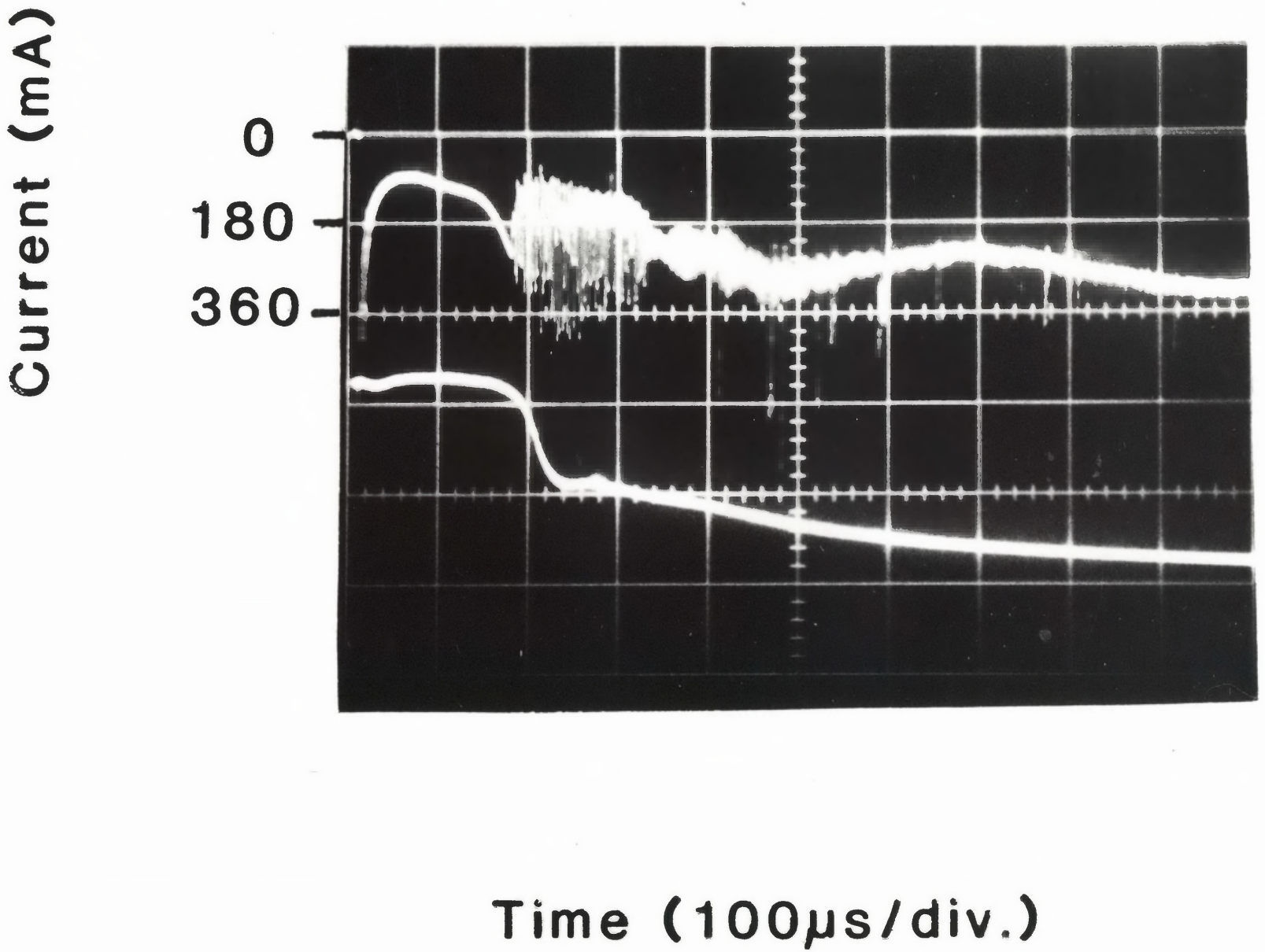
Current (mA)
0
180
360
Time (100μs/div.)

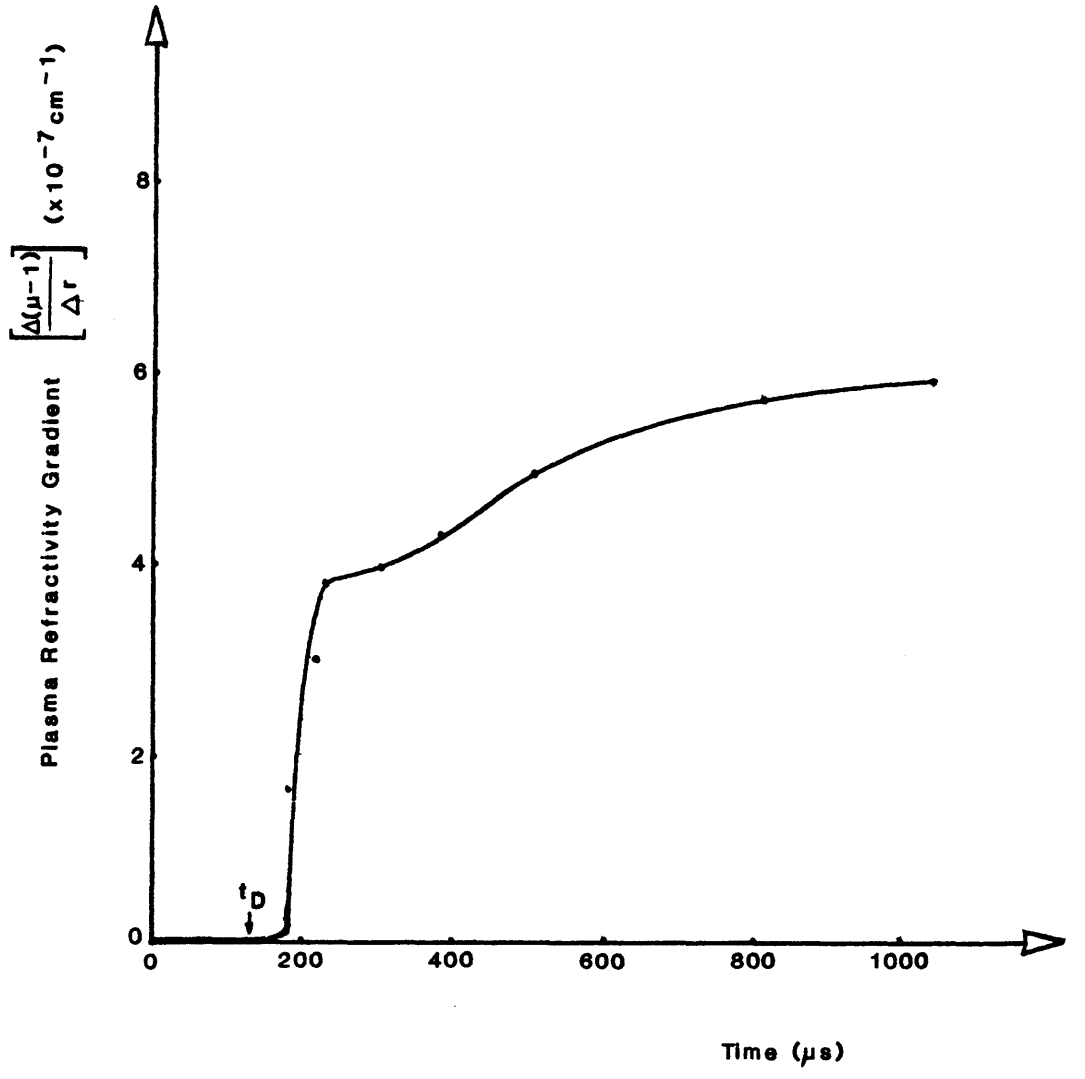

Fig. 3.2.4.(ii) Graph of plasma refractivity gradient as a function of time during the growth of a 0.55 Torr SF_6 spark pulsed at 10.0 kV in the metre-tube. The Jamin interferometer laser beams were located at 6 mm and 10 mm from the tube axis. The uncertainty at every point of the curve is $\pm$ 9.5 x 10^{-8} cm^{-1}.

This assumes that a shift of more than one full fringe has not occurred. As can be seen from the present interferometric trace, less than a full fringe has passed the photomultiplier slit over the duration of the spark. The accuracy with which this trace can be read is 0.02 volts, thus giving a fringe shift accuracy of 0.06 of a fringe from equation 3.2.4g. From a knowledge of the fractional fringe shift δ, the radial plasma refractivity gradient averaged over the radial distance $\Delta r = 4$ mm in the range $6.0 \text{ mm} \leqslant r \leqslant 10.0 \text{ mm}$, and also averaged over the length of the plasma, can be determined by dividing equation 2.3.2a by Δr and rearranging to give

$$\frac{\Delta(\mu-1)}{\Delta r} = \frac{\delta\lambda}{L\Delta r} \qquad (3.2.4h).$$

This gradient has been plotted as a function of time during spark growth and is shown in Fig. 3.2.4.(ii). The uncertainty of every point on the graph is $\pm 9.5 \times 10^{-8}$ cm^{-1}. By substituting the expression for δ given in equation 2.3.2e into equation 3.2.4h and rearranging terms, the radial molecular density gradient $\frac{\Delta N}{\Delta r}$ is

$$\frac{\Delta N}{\Delta r} = \frac{1}{K} \frac{\Delta(\mu-1)}{\Delta r} \qquad (3.2.4i)$$

where K is equal to 2.91×10^{-23} cm^3 (see Section 2.3.2.(i)). $\frac{\Delta N}{\Delta r}$ can thus be plotted as a function of time, so long as only the ground state SF_6 molecules contribute to the discharge refractivity. The reason $\frac{\Delta N}{\Delta r}$ has not been plotted is because as indicated earlier, molecular dissociation becomes important after time t_D, so that other species have then to be taken account of.

The interpretation of Fig. 3.2.4.(ii) will be postponed until Section 3.2.7, while the measurements of absolute plasma refractivity will now be presented.

3.2.4.(iii) The Lee-Woolsey interferometer measurements

The Lee-Woolsey interferometer was set up as explained in Section 2.3.2.(iii) about the metre discharge tube and the desired radial position of the scene beam set by rotating the lead screw of the interferometer table which houses the input section. To facilitate interferogram analysis, the photomultiplier signal amplitude corresponding to the peak-to-peak fringe intensity was recorded prior to each discharge shot on the oscillogram upon which the interferometer trace was to be obtained. This was done by disengaging the

oscilloscope time-base and strongly tapping one of the interferometer tables, so that multiple fringes would sweep across the detector. By keeping the oscilloscope camera shutter open during this procedure, a vertical line representing the peak-to-peak fringe intensity was recorded on the camera film.

The discharge chamber was filled with SF_6 to a pressure of 0.80 Torr after being evacuated to less than 10^{-4} Torr. The gap was then pulsed at 12.00 kV, as indicated before, and an oscillogram of the interferometer trace and corresponding current trace was obtained for the entire duration of spark growth and decay. A typical oscillogram for the case of an axial scene beam is shown in Fig. 3.2.4.(iii) where the upper waveform is the interferometric trace. Here, zero fringe intensity, corresponding to the middle of a dark fringe, occurs at the top of the vertical white line. The stability of the Lee-Woolsey interferometer enables the fringe pattern to be adjusted so that the detector lies midway between maximum and minimum fringe intensity before the discharge is pulsed. Observation of the interferogram obtained then clearly indicates the direction of fringe movement across the detector upon firing the discharge. By previously observing the direction of fringe movement when a little gas is admitted to the discharge chamber, the direction of trace movement can thus be directly related to an increase or decrease in N.

If during discharge development, a large fluctuation occurs in the average number density along the scene beam, multiple fringes will cross the detector aperture until such time as the density begins to change in the opposite direction. When this occurs, a "saddle-point" will be observed on the interferogram due to a reversal in the direction of fringe sweep. When a saddle-point occurs midway between the fringe extrema, it is very conspicuous. When it occurs on the other hand at or close to a fringe extremum it is not distinguishable from a turnover point caused by a fringe sweep in a single direction. This zero sensitivity occurring in the middle of a bright or dark fringe could thus lead to ambiguous results. Hence whenever this problem was encountered in the present experiments, the fringe pattern was re-adjusted

Fig. 3.2.4.(iii) Oscillogram showing the Lee-Woolsey interferometer trace (upper) and current trace (lower) for a 0.80 Torr SF_6 spark pulsed in the metre-gap at 12.00 kV, and at an overvoltage of 120%.
The interferometer trace is obtained with the scene-beam located axially along the discharge tube.

Fig. 3.2.4.(iv) Oscillogram showing the same traces shown in Fig. 3.2.4.(iii) on a much slower sweep speed.

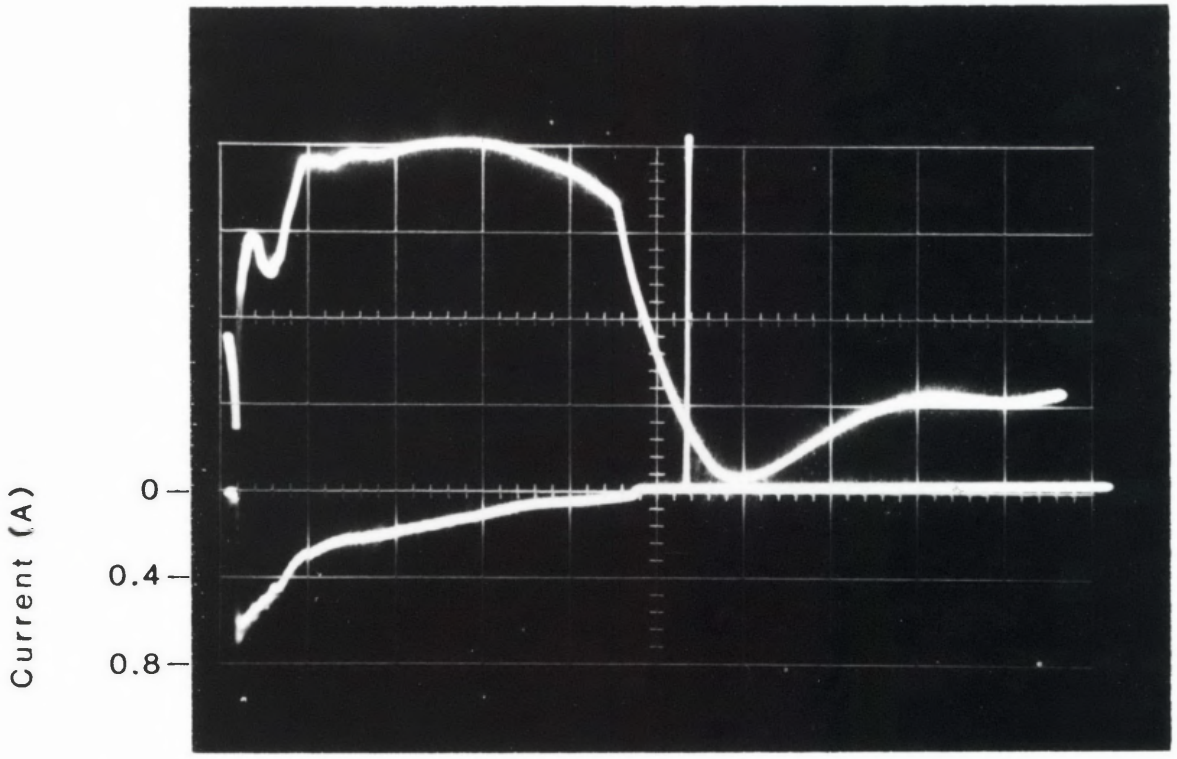

Time (5ms/div.)

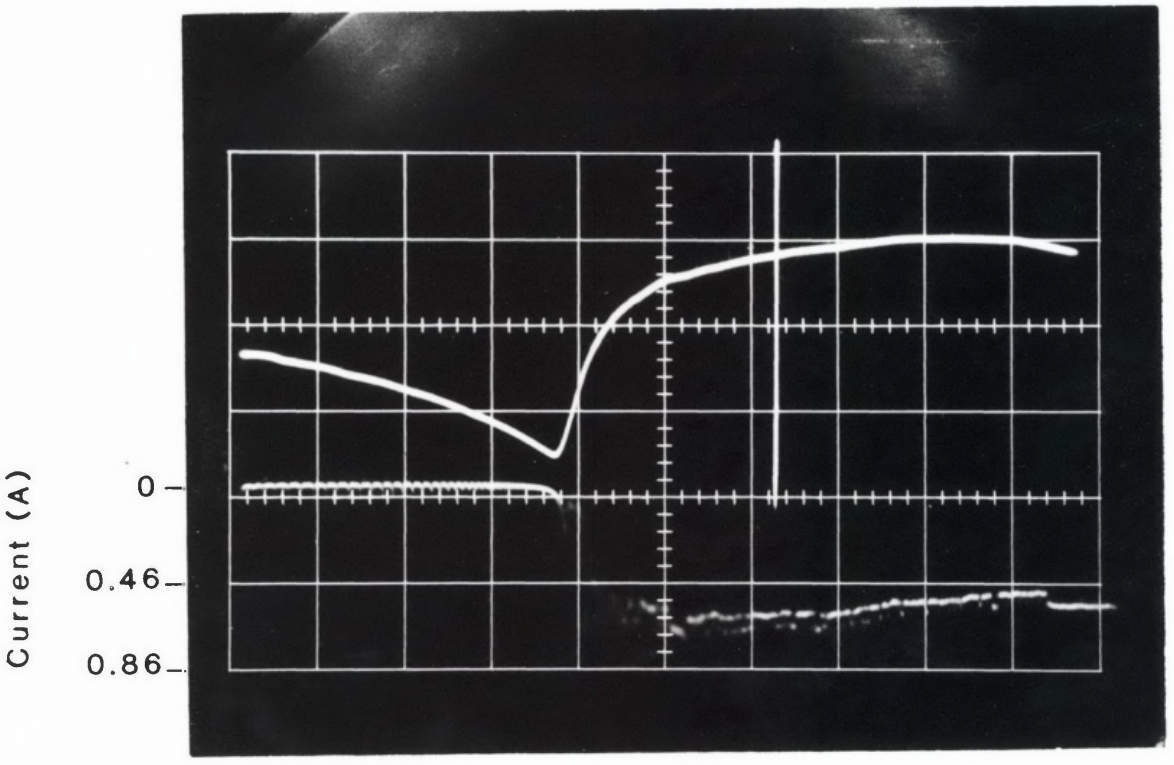

Time (200μs/div.)

with respect to the photodetector such that the saddle-point occurred away from the fringe extrema.

The analysis of the interferometer traces in terms of fringe shifts is basically similar to that used for the Jamin trace. However, since many traces have required analysis in this work, it has been found that rather than measuring all trace amplitudes with respect to that at time zero, it is easier to measure all values with respect to an arbitrary axis corresponding to one of the oscilloscope graticule lines. The fringe intensity distribution is of the $(\text{cosine})^2$ form given by equation 3.2.4e. It can thus be shown that the fractional fringe shift δ, in moving from an initial point with vertical coordinate y_0 (with respect to an arbitrary axis) to a point with coordinate y (with respect to the same axis), is

$$\delta = \frac{1}{\pi}\left[\cos^{-1}\left\{\frac{y-\ell}{A}\right\}^{\frac{1}{2}} - \cos^{-1}\left\{\frac{y_0-\ell}{A}\right\}^{\frac{1}{2}}\right] \qquad (3.2.4j)$$

where ℓ is the coordinate of the lower extremum (zero intensity) with respect to the arbitrary axis and

$$A = u - \ell \qquad (3.2.4k)$$

where u is the corresponding coordinate of the upper extremum. Equation 3.2.4j assumes that no turnover point corresponding to an intensity maximum or minimum has been passed. If this does occur, the required fractional fringe is added.

The interferometer trace is analysed by substituting the value of y at any given time into equation 3.2.4j and calculating the fringe shift. The change in discharge refractivity $\Delta(\mu-1)$ can thus be calculated from equation 2.3.2a for different times, from which changes in gas number density can be determined using equation 2.3.2d, as long as it can be assumed that only the SF_6 gas molecules contribute to the total plasma refractivity. By substituting the minimum resolvable y- value of the interferometer trace into equation 3.2.4j, a minimum resolvable fringe shift of one-hundredth of a fringe is obtained.

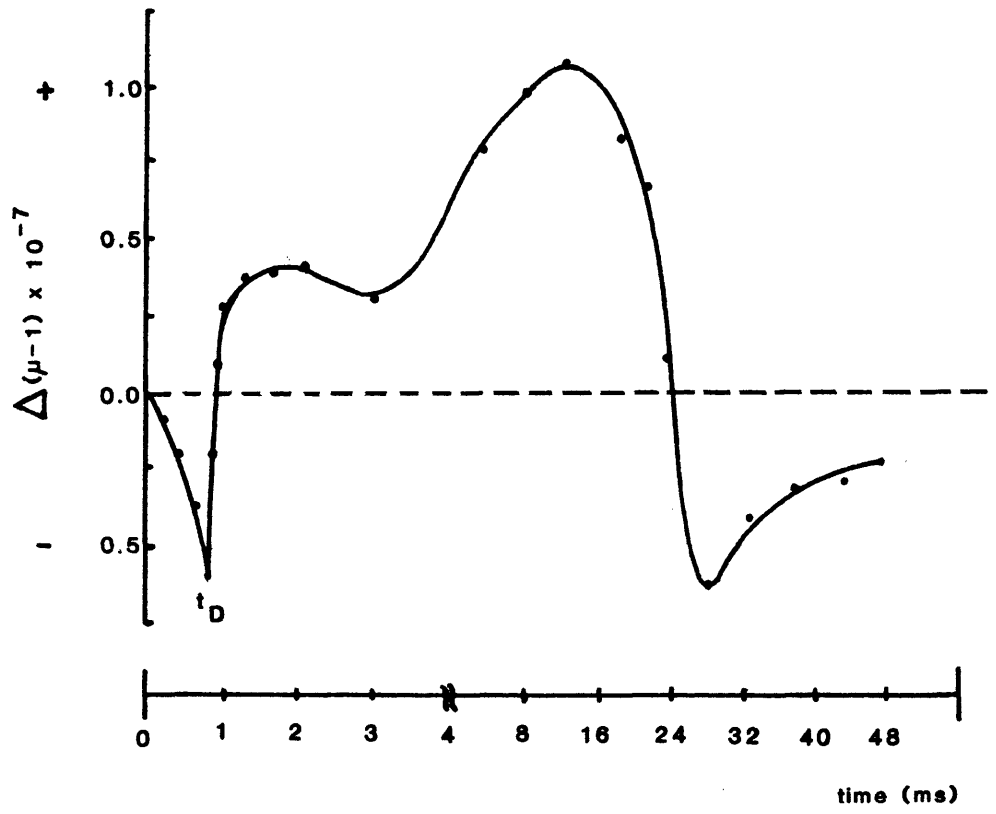

Fig. 3.2.4.(v) Graph of the change in absolute plasma refractivity from the initial value at time t_o, as a function of time during the growth and decay of a 0.80 Torr, 12.00 kV SF_6 spark pulsed in the metre-gap. The graph represents absolute refractivity changes along the discharge tube axis. Note that the time-scale is broken at 4 ms.

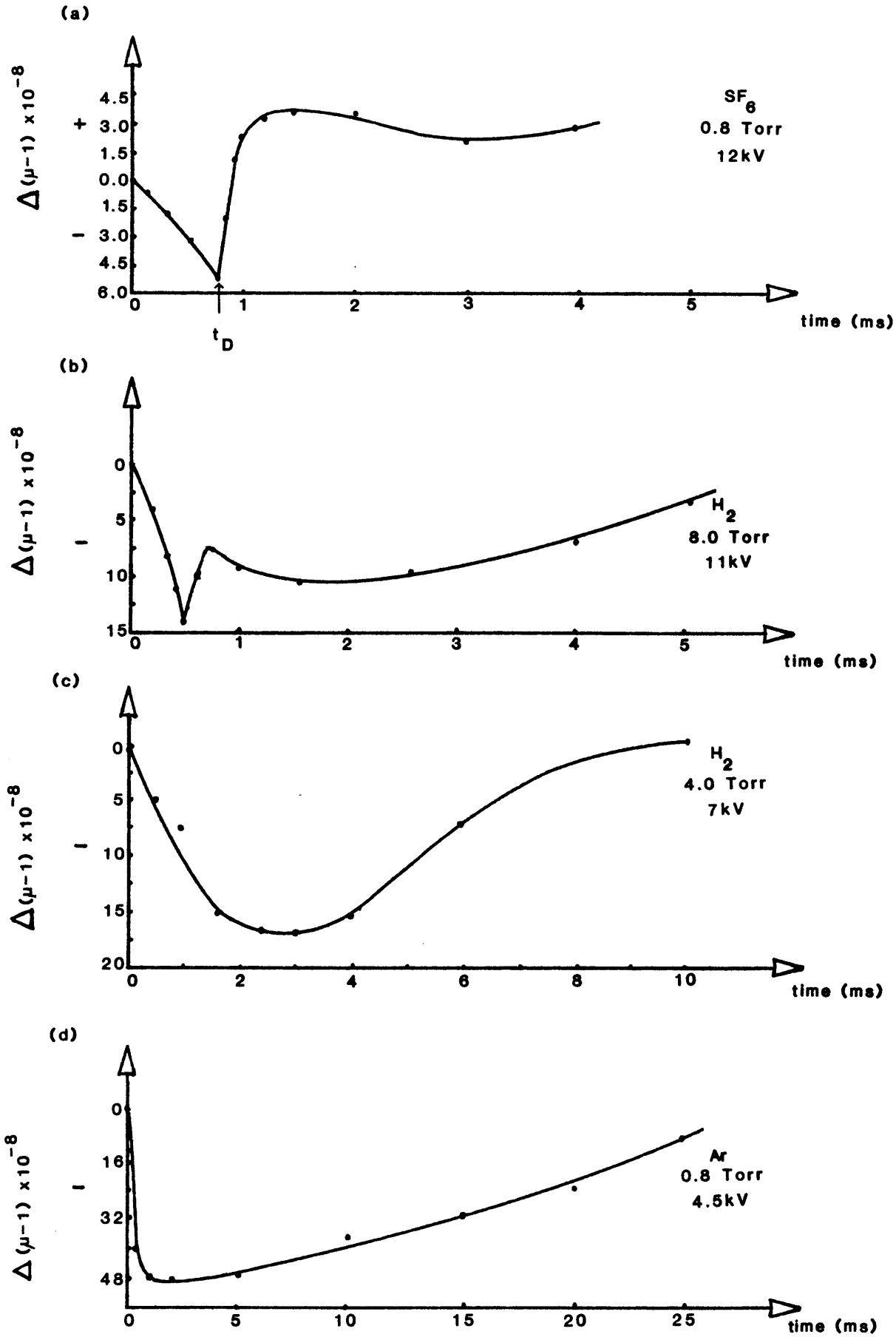

Fig. 3.2.4.(vi) Variations in axial plasma refractivity as a function of time in hydrogen and argon sparks pulsed in the metre-gap under different conditions of applied voltage and pressure. The SF_6 curve of Fig. 3.2.4.(v) has been re-drawn, and included for comparison.

Figure 3.2.4.(iv) shows interferometer- and current-traces for the same discharge as Fig. 3.2.4.(iii) also using an axial scene beam. The time scale has been expanded to show the interferometer trace in the early stages of development. A graph of the change in axial plasma refractivity as a function of time has been plotted in Fig. 3.2.4.(v). The most important and interesting features appear in approximately the first four milliseconds of discharge evolution. This time interval has thus been expanded on the graph of Fig. 3.2.4.(v). Each division of the vertical scale is a change in discharge refractivity, $\Delta(\mu-1)$, of 2.5×10^{-8}. So long as the neutral SF_6 remains the dominant contributor to the discharge refractivity (which it does until time t_D), this value corresponds to a change in SF_6 molecular number density of 8.6×10^{14} cm^{-3}. This in turn is equivalent to a change of 3.26% per division from the equilibrium number density of 2.64×10^{16} cm^{-3}. The horizontal broken line on the graph represents the initial gas refractivity.

The temporal variations in plasma refractivity obtained for different radial positions up to 8 mm off axis, are of approximately similar profile to the axial plot of Fig. 3.2.4.(v), for times within 2 ms of breakdown.

To aid interpretation of refractivity variations (and hence number density variations) in the SF_6 spark, it was found desirable, for reasons to be discussed in Section 3.2.7, to compare the behaviour of transient plasmas of other gases with that of SF_6. Thus interferograms for the case of an axial scene beam were obtained for 8 Torr and 4 Torr hydrogen sparks pulsed at 11 kV and 7 kV respectively and for a 0.8 Torr argon spark fired at 4.5 kV. From these interferograms, changes in axial discharge refractivity were obtained as a function of time and are shown in Fig. 3.2.4.(vi). A portion of the axial plot for SF_6 is also shown in this figure for comparison.

3.2.5 The Space-Charge Phase, $t_A - t_B$

When breakdown occurs at time t_A, ionization growth in the SF_6 spark is likely to proceed chiefly through the dissociative ionization process,

$$e + SF_6 \rightarrow SF_5^+ + F + 2e \qquad (1.3.3a)$$

according to the results of Dibeler and Mohler (1948) (see Section 1.3.3.(i)).

The ionization rate of the SF_6 molecules is extremely low in comparison to the rate of process 1.3.3a; and other ionization processes which produce positive ions such as SF_3^+ and SF_4^+, can be ignored at the low mean electron energies (< 15 eV) found in the present experiments.

The rate of current growth will be retarded from the time of breakdown by diffusion losses and primary and secondary attachment processes, and will also be affected by detachment and charge-transfer (i.e. electron-transfer) reactions such as those discussed in Section 1.3.3.

As seen in every oscillogram shown in the previous sections, the growth of current is very rapid after breakdown, but is suddenly arrested at time t_B. The duration of the interval t_A-t_B is difficult to resolve on these oscillograms, but is observed to be approximately 400 ns in the case of Figures 3.2.3.(i) and 3.2.2.(iv)a, using higher time-resolution.

As the current starts to grow, a positive-ion space-charge sheath rapidly develops adjacent to the cathode and a large cathode fall in potential is established. Because of this, the axial field in the rest of the gap (except very close to the anode) collapses from the applied value. At time t_B, the measured positive column field in the 1.6 Torr, 3 kV spark is (120 ± 25) Vcm^{-1} as indicated in Fig. 3.2.3.(ii). An estimate can be made of the corresponding field in the 0.8 Torr, 12 kV spark, by assuming a cathode fall similar to that obtained at time t_B in the former spark. This assumption is not unreasonable since the currents flowing in both sparks at time t_B are of similar magnitude (252 mA in the 0.8 Torr, 12 kV spark and 310 mA in the 1.6 Torr, 3 kV spark), and further since the cathode fall appears to be relatively insensitive to changes in discharge current over this range. For example, Fig. 3.2.3.(ii) shows that the cathode fall changes by only 150 volts for currents between 53 mA and 320 mA. Therefore, taking a cathode fall of 1350 V (see Fig. 3.2.3.(ii)) and a total gap voltage of 9500 V at time t_B in the metre-spark (as measured from Fig. 3.2.2.(iv)a), a column field of approximately 82 Vcm^{-1} is obtained. In any case, it turns out that even if the cathode fall in the metre-tube differed from the assumed value by as much as 50%, the column field would

still lie within 10% of the value just quoted.

In conjunction with the above field measurements, the interferometric measurements described in Section 3.2.4.(iii) provide some information on the space-charge phase. Observation of Fig. 3.2.4.(v) shows that in the phases immediately following breakdown, the SF_6 number density falls in the axial region. This decrease occurs in response to the development of a radial temperature gradient in the discharge tube. Nevertheless it can be seen that the decrease in axial N is still negligible (< 1%) at time t_B in the 0.8 Torr, 12 kV spark. This observation was checked, using a photomultiplier tube in place of the photodiode used in these measurements (see Section 2.3.2.(iii)) since the rise-time of the latter detector will have been too slow to register a rapid change in number density during the space-charge phase, if this did occur. However, the interferometric traces obtained with the photomultiplier were exactly the same as the photodiode traces, confirming that the decrease in axial N at time t_B was in fact less than 1%. This information suggests therefore, that the column E/N at time t_B in the 0.8 Torr, 12 kV spark is approximately 313 Td. (taking N at that time to be 2.61×10^{16} cm^{-3}). As for the 1.6 Torr, 3 kV spark it could be assumed that the decrease in axial N would also be within a few per cent at time t_B in view of (i) the negligible amount of energy fed to the spark up to this time, and (ii) the long diffusion times in SF_6. If this assumption is correct, the column E/N in this spark at time t_B will be approximately 230 Td. (taking N to be 5.22×10^{16} cm^{-3}).

The above values of E/N in the two sparks at time t_B are considerably lower than the 'critical value' discussed in Section 1.3.3. There it was pointed out that when attachment is the only significant electron loss process, the critical E/N (under equilibrium conditions) at which the rates of electron production and loss are equal, is 362 Td. Here, wall diffusion as well as electron attachment are significant loss processes, so that the critical E/N must be greater than 362 Td.

At time t_A, the applied E/N-value is considerably higher than the critical value so that λ/N (the net ionization coefficient) assumes some large positive value, and the current rapidly grows. A specific value for λ/N at time t_A cannot be estimated from the applied E/N-value however, since equilibrium between the electrons and the electric field is unlikely to have been achieved at this time.

The fact that E/N falls below the critical value before time t_B, suggests that the electrons do not attain equilibrium with the field at any time before time t_B. As the current grows, λ/N (and hence the rate of current growth) must eventually decrease due to the fall in E/N. As soon as the net electron production rate (which takes attachment into account) falls below the diffusion loss rate at time t_B, the current rapidly falls (electron-ion recombination losses can be neglected at these low pressures (von Engel, 1965)).

As expected, the current amplitude attained at time t_B decreases with decreasing applied E/N (see Figures 3.2.2.(iii) and (iv)).

3.2.6.I The Electronegative Glow Phase, $t_B - t_D$

The current fall regime from time t_B to t_C and the ensuing low-current phase from time t_C to t_D have been collectively called the electronegative glow phase due to the significance of electron attachment during these periods. Some experimental evidence suggesting electron attachment in this regime will be presented later in this section and also in Section 3.2.8.

From the electric field measurments described earlier, the cathode fall voltage appears to decrease from (1350 ± 125) V at time t_B to (1250 ± 150) V at time t_o + 100 μs, in the 1.6 Torr, 3 kV SF_6 spark. Simultaneously, the positive column field increases from (120 ± 25) Vcm^{-1} at time t_B to (168 ± 25) Vcm^{-1} at $t = t_o$ + 100 μs (see Figures 3.2.3.(i) and (ii)).

If a similar cathode fall to that found in the low-current phase of the above spark (i.e. 1250 V) can be assumed to exist in the corresponding phase of the 0.8 Torr, 12 kV, 1 metre spark, then the column field in the latter spark will be approximately 102 Vcm^{-1} during the low-current phase (taking

the total gap voltage to be 11.4 kV, as measured from Fig. 3.2.2.(iv)a). This is an increase of about 22% from the value estimated for time t_B.

The decrease in the axial SF_6 number density can be seen from Fig. 3.2.4.(v) to be still negligible at time t_C, so that the E/N-value at this time in the 0.8 Torr, 12 kV spark must be approximately 392 Td. (taking N to be 2.60 x 10^{16} cm^{-3} at time t_C). In the 1.6 Torr, 3 kV spark, the decrease in axial N might be expected to be somewhat greater at time t_C, as suggested by the higher currents (compare Figures 3.2.3.(i) and 3.2.2.(iv)a).

The increase in E/N through the current fall regime brings about an increase in the net ionization coefficient λ/N and hence a decrease in the rate of current fall. When E/N eventually attains the critical value at which the net electron production rate balances the diffusion loss rate, the discharge settles into the low-current phase. As calculated above, this critical E/N is approximately 392 Td for the above spark in the metre-tube, where diffusion losses will be significant. For the 1.6 Torr, 3 kV spark, calculation shows that the decrease in axial N at time t_C must be at least 12% in order that E/N at that time be greater than 362 Td.

Figures 3.2.2.(iii) and (iv) show how the amplitude of the low current phase increases with higher applied overvoltage, as expected, whilst the duration decreases. The explanation for the latter effect will be presented in Section 3.2.7 where the transition out of the low-current phase will be discussed. The amplitude of the low-current phase does not remain constant with time, but gradually increases from t_C to t_D (see for example Fig. 3.2.3.(i)), this effect becoming more pronounced as the applied E/N is raised. This increase in current amplitude can be accounted for by the continued decrease in axial N, and hence by the rise in axial E/N throughout the phase. It can be seen for example from Fig. 3.2.4.(v) that for the 0.8 Torr, 12 kV spark pulsed in the metre-gap, the decrease in axial gas refractivity by the end of the low current phase is about 6 x 10^{-8}, which corresponds to a decrease in the axial SF_6 number density of 2.1 x 10^{-15} cm^{-3}. This is a drop of about 8% from the initial density.

It seems likely that the reason why the current falls at time t_B is because the rate of electron attachment increases as the column field drops in the space-charge regime. At the values of E/N measured at time t_B, electron attachment is a dominant process. It is thus expected that the behaviour of the discharge in the current-fall and low-current regimes is dominated by electron-attachment processes.

Useful information has been obtained on the extent of electron attachment in d.c. SF_6 discharges under conditions somewhat similar to the quasi-stable low-current spark phase. For example, in a 2.5 Torr SF_6 discharge at 1 mA, the negative ion-to-electron number density ratio has been found, using Langmuir probe analysis, to be in excess of 5×10^3:1. These investigations will be discussed in more detail in Section 3.2.6.II.

In view of the relatively low E/N in the low current phase, it is speculated that the negative ion species found in the spark channel during this regime are SF_6^-, SF_5^- and F^-. However, on the basis of discussions in Section 1.3.3.(ii) it cannot be expected that the relative abundances of these species will be the same as those observed by Compton *et al.* (1971) and McGeehan *et al.* (1975) at similar E/N, under pre-breakdown conditions. In the low-current phase, the currents are obviously much higher than in the pre-breakdown regime (mA as opposed to nA/μA) and the gas temperatures are generally higher as well. Thus the pre-breakdown data can only be used as an approximate guide in the discussion of post-breakdown phenomena. Nevertheless, it can be expected that as the E/N-ratio is increased in the low-current glow discharge, and as the gas temperature exceeds about 600 K (refer to Section 1.3.3.(ii)), the F^- abundance will increase at the expense of SF_5^- and SF_6^-.